

Long waves through emergent coastal vegetation

Chan, I-Chi; Huang, Zhenhua; Zhang, Wenbin; Mei, Chiang C.; Liu, Philip L. F.

2011

Mei, C. C., Chan, I. C., Liu, P. L. F., Huang, Z., & Zhang, W. (2011). Long waves through emergent coastal vegetation. *Journal of Fluid Mechanics*, 687, 461-491.

<https://hdl.handle.net/10356/95302>

<https://doi.org/10.1017/jfm.2011.373>

© 2011 Cambridge University Press. This paper was published in *Journal of Fluid Mechanics* and is made available as an electronic reprint (preprint) with permission of Cambridge University Press. The paper can be found at the following official URL: [<http://dx.doi.org/10.1017/jfm.2011.373>]. One print or electronic copy may be made for personal use only. Systematic or multiple reproduction, distribution to multiple locations via electronic or other means, duplication of any material in this paper for a fee or for commercial purposes, or modification of the content of the paper is prohibited and is subject to penalties under law."

Downloaded on 20 Mar 2024 18:24:36 SGT

Long waves through emergent coastal vegetation

Chiang C. Mei^{1,2,†}, I-Chi Chan², Philip L.-F. Liu^{2,3}, Zhenhua Huang⁴
and Wenbin Zhang⁴

¹ Department of Civil and Environmental Engineering, Massachusetts Institute of Technology, Cambridge, MA 02139, USA

² School of Civil and Environmental Engineering, Cornell University, Ithaca, NY 14853, USA

³ Institute of Hydrological and Oceanic Sciences, National Central University, Zhongli, Taiwan, 32001

⁴ Earth Observatory of Singapore and Department of Civil and Environmental Engineering, Nanyang Technological University, Singapore 639398

(Received 26 December 2010; revised 14 July 2011; accepted 5 September 2011;
first published online 14 October 2011)

We study the effects of emergent coastal forests on the propagation of long surface waves of small amplitude. The forest is idealized by an array of vertical cylinders. Simple models are employed to represent bed friction and to simulate turbulence generated by flow through the tree trunks. A multi-scale (homogenization) analysis similar to that for seepage flows is carried out to deduce the effective equations on the macro-scale. The effective coefficients are calculated by numerically solving the micro-scale problem in a unit cell surrounding one or several cylinders. Analytical and numerical solutions for wave attenuation on the macro-scale for different bathymetries and coastal forest configurations are presented. For a transient incident wave, analytical results are discussed for the damping of a leading tsunami. For comparison series of laboratory data for periodic and transient incident waves are also presented. Good agreement is found even though some of the measured waves are short or nonlinear.

Key words: shallow water flows, surface gravity waves, wave–turbulence interactions

1. Introduction

The hydrodynamics of tidal flows through mangrove swamps have been widely studied to understand the health of coastal ecosystems (see Wolanski, Jones & Bunt 1980; Wolanski 1992; Mazda, Kobashi & Okada 2005). For inland waters, Nepf (1999) has investigated transport and diffusion of nutrients and solvents in a steady current. It has also been noted that coastal forests can serve as barriers against tides, storm surges and tsunami waves. Historical evidence suggests that mangroves shielded the Eastern coast of India and reduced the number of deaths in the 1999 cyclone attack (Dasa & Vincent 2009). Records of the 2004 Indian Ocean tsunami have given strong support to the idea of shore protection by mangroves and trees (Danielsen *et al.* 2005; Tanaka *et al.* 2007). Field experiments conducted in Australia and Japan have demonstrated that during high tides only 50 % of incident wave energy is transmitted

† Email address for correspondence: ccmei@mit.edu

through forests over a distance of 200 m (Massel, Furukawa & Binkman 1999). This evidence has motivated suggestions for laboratory studies of planting a strip of trees along shores. For instance, Hiraishi & Harada (2003) have proposed the *Green Belt* with trees planted in water. Similarly, Irttem *et al.* (2009) have shown experimentally that trees planted on the landward side of the shore can reduce the maximum run-up of a model tsunami by as much as 45 %. On the other hand, short wind waves through salt marshes have been studied in the laboratory by Augustin, Irish & Lynett (2009), Kobayashi, Raichlen & Asano (1993) and Suzuki, Dijkstra & Stive (2008), and in the field by, for example, Möller *et al.* (1999) and Möller (2006). Also, Fernando *et al.* (2008) and Thuy *et al.* (2009) have examined the significant enhancement of tsunami height in an open gap between coral reefs in Sumatra. Various models of numerical simulations have been proposed by these authors based on assumed equations for the macro-scale (wavelength) motion and empirically fitted coefficients.

In tidal swamps, part or most of the vegetation may be constantly immersed in water. For effective protection against tsunamis, the thickness of the green forest needed can be hundreds of metres. Hence submerged plantation would probably be a more preferred option along well-populated shores. In this article, we describe a micro-mechanical theory for the propagation and dissipation process of long waves through emergent vegetation.

The dissipation of wave energy is dominated by turbulence generated between the tree trunks, branches and leaves throughout the entire sea depth, and by bed friction (Massel *et al.* 1999). To avoid massive computations, a number of simplifications are made here to enable an analysis of the macro-scale phenomenon from the micro-scale upwards. The first is to limit considerations to long waves of small amplitude so that a linearized approximation applies. The second is to use the model of constant eddy viscosity with values taken from past experiments for steady flows through vegetated waters. Bottom friction is modelled by a linear term with an empirical friction coefficient. Finally, only the effects of tree trunks are modelled by vertical cylinders in a periodic array. With these simplifications the two-scale method of homogenization is carried out to derive the macro-scale equations which are reminiscent of those governing seepage flows in porous media. The effective hydraulic conductivity, which quantifies the effects of tree trunks on the mean flows, is calculated from the solution of an initial-boundary-value problem on the micro-scale. Then several macro-scale problems are solved analytically for different incident wave conditions and coastal forest configurations. A series of laboratory experiments is also carried out for both periodic and transient incident waves. Comparisons of measurements and numerical simulations are discussed.

2. Formulation

Let $\mathbf{x} = (x_1, x_2)$ denote the horizontal coordinates and z represent the vertical direction. We consider a shallow sea of water depth $h(\mathbf{x})$ which varies over a distance scale comparable to a wavelength. Over a large horizontal area, vertical cylinders are planted as a periodic array to represent trees. Infinitesimal long waves enter the emergent vegetation from the open sea. The tree spacing ℓ and the typical water depth h_0 are comparable to but much smaller than the typical wavelength $O(1/k_0)$, i.e. $k_0\ell = O(k_0h_0) \ll 1$. The characteristic wavenumber k_0 is related to the frequency ω by $k_0 = \omega/\sqrt{gh_0}$, where g is the gravitational acceleration.

2.1. Linearized equations

Under the assumption of constant eddy viscosity and infinitesimal waves, the three-dimension flow between the trees are governed by the linearized Reynolds equations:

$$\frac{\partial u_i}{\partial x_i} + \frac{\partial w}{\partial z} = 0, \quad i = 1, 2, \quad (2.1)$$

and

$$\frac{\partial u_i}{\partial t} = -\frac{1}{\rho} \frac{\partial p}{\partial x_i} + \nu_e \left(\frac{\partial^2 u_i}{\partial x_j \partial x_j} + \frac{\partial^2 u_i}{\partial z^2} \right), \quad i, j = 1, 2. \quad (2.2)$$

In the above, u_i and w are the horizontal and vertical velocity components respectively, ρ denotes the density, ν_e is the eddy viscosity, and p represents the dynamic pressure so that the total pressure is

$$P = p - \rho g z. \quad (2.3)$$

No-slip boundary conditions are imposed on the seabed,

$$u_i = w = 0, \quad z = -h(\mathbf{x}), \quad (2.4)$$

and on the cylinders,

$$u_i = w = 0, \quad (\mathbf{x}, z) \in S_B. \quad (2.5)$$

The kinematic condition on the mean free surface is

$$\frac{\partial \eta}{\partial t} = w, \quad z = 0, \quad (2.6)$$

where η denotes the free-surface displacement. For the dynamic conditions on the free surface, we require the vanishing of both the normal and tangential stresses, hence

$$g\eta - \frac{p}{\rho} + 2\nu_e \frac{\partial w}{\partial z} = 0, \quad z = 0, \quad (2.7)$$

and

$$\frac{\partial u_i}{\partial z} + \frac{\partial w}{\partial x_i} = 0, \quad z = 0. \quad (2.8)$$

2.2. Depth-averaged equations

The incoming waves dictate the size of the dynamic pressure scale $[p] = \rho g A$, where A denotes the typical wave amplitude. The corresponding horizontal gradient is $k_0[p]$. We regard the typical wavelength, $1/k_0$, as the characteristic macro-length scale, and the tree spacing, ℓ , as the micro-length scale. Using ℓ and h_0 to normalize the spatial coordinates and the inverse of characteristic frequency, $1/\omega$, as the time scale, we introduce the following dimensionless variables:

$$\begin{aligned} x_i^* &= \frac{x_i}{\ell}, & z^* &= \frac{z}{h_0}, & t^* &= t\omega, & h^* &= \frac{h}{h_0}, \\ \eta^* &= \frac{\eta}{A}, & p^* &= \frac{p}{\rho g A}, & u_i^* &= \frac{u_i}{\sqrt{gh_0 A}/h_0}, & w^* &= \frac{w}{A\omega}. \end{aligned} \quad (2.9)$$

The normalized equations are

$$\frac{\partial u_i^*}{\partial x_i^*} + \epsilon \frac{\partial w^*}{\partial z^*} = 0, \quad (2.10)$$

$$\epsilon \frac{\partial u_i^*}{\partial t^*} = -\frac{\partial p^*}{\partial x_i^*} + \epsilon \sigma \left[\frac{\partial^2 u_i^*}{\partial x_j^* \partial x_j^*} + \left(\frac{\ell}{h_0} \right)^2 \frac{\partial^2 u_i^*}{\partial z^* \partial z^*} \right], \quad (2.11)$$

where

$$\epsilon \equiv k_0 \ell = \frac{\omega \ell}{\sqrt{g h_0}} \ll 1 \quad (2.12)$$

is the small ratio of micro-to-macro length scales, $\ell/h_0 = O(1)$, and

$$\sigma = \frac{v_e}{\omega \ell^2} \quad (2.13)$$

is the square of the ratio of turbulent diffusion length to tree spacing. Note that σ can take a wide range of values including $O(1)$ and is larger for longer waves or denser forests.

The dimensionless boundary conditions on the free surface are

$$\frac{\partial \eta^*}{\partial t^*} = w^*, \quad z^* = 0, \quad (2.14)$$

and

$$\eta^* - p^* + 2\epsilon^2 \sigma \frac{\partial w^*}{\partial z^*} = 0, \quad z^* = 0, \quad (2.15)$$

$$\frac{\partial u_i^*}{\partial z^*} + \epsilon \left(\frac{h_0}{\ell} \right)^2 \frac{\partial w^*}{\partial x_i^*} = 0, \quad z^* = 0. \quad (2.16)$$

Denoting by an overbar the depth-average,

$$\bar{\mathcal{F}} = \frac{1}{h^*(\mathbf{x}^*)} \int_{-h^*}^0 \mathcal{F} \, dz^*, \quad (2.17)$$

we have from (2.10)

$$\frac{\partial(h^* \bar{u}_i^*)}{\partial x_i^*} + \epsilon \frac{\partial \eta^*}{\partial t^*} = 0. \quad (2.18)$$

Use is made of (2.4), (2.6) and the assumption that $h = h(\mathbf{x})$ varies significantly over the distance $O(1/k_0)$ only, but not over $O(\ell)$.

By similar depth-averaging of (2.11), we get

$$\epsilon \frac{\partial \bar{u}_i^*}{\partial t^*} = -\frac{\partial \eta^*}{\partial x_i^*} + \epsilon \sigma \frac{\partial^2 \bar{u}_i^*}{\partial x_j^* \partial x_j^*} + \epsilon \frac{\sigma}{h^*} \left(\frac{\ell}{h_0} \right)^2 \left[\frac{\partial u_i^*}{\partial z^*} \right]_{-h^*}^0, \quad (2.19)$$

where the long-wave assumption has been made. We further represent the bottom shear by a linear term,

$$\frac{\sigma}{h^*} \left(\frac{\ell}{h_0} \right)^2 \left[\frac{\partial u_i^*}{\partial z^*} \right]_{-h^*}^0 \equiv \alpha \bar{u}_i^*, \quad (2.20)$$

which defines α . Equation (2.19) becomes

$$\epsilon \frac{\partial \bar{u}_i^*}{\partial t^*} = -\frac{\partial \eta^*}{\partial x_i^*} + \epsilon \sigma \frac{\partial^2 \bar{u}_i^*}{\partial x_j^* \partial x_j^*} - \epsilon \alpha \bar{u}_i^*. \quad (2.21)$$

In physical units, (2.18) and (2.21) are

$$\frac{\partial(h\bar{u}_i)}{\partial x_i} + \frac{\partial \eta}{\partial t} = 0, \quad (2.22)$$

$$\frac{\partial \bar{u}_i}{\partial t} = -g \frac{\partial \eta}{\partial x_i} + \nu_e \frac{\partial^2 \bar{u}_i}{\partial x_j \partial x_j} - f \bar{u}_i, \quad (2.23)$$

where f is the bed friction coefficient and $\alpha = f/\omega$. The bottom shear stress, (2.20), becomes

$$\nu_e \left[\frac{\partial u_i}{\partial z} \right]_{-h} = f \bar{u}_i h. \quad (2.24)$$

Both parameters ν_e and f (or σ and α in the dimensionless form) are given by empirical formulae to be discussed shortly.

2.3. Estimation of controlling parameters

In the absence of direct measurements of momentum diffusivity in transient flows through a cylinder array, we shall use the empirical diffusivity for steady flows through emergent vegetation obtained from extensive tests by Nepf (1999) who also collected other field data for a moderate range of Reynolds number, $Re_d = U_0 d/\nu = 400\text{--}2000$, where ν is the molecular kinematic viscosity of water, U_0 the characteristic velocity and d the diameter of the cylinders. From her figure 10, the turbulent diffusivity, ν_e , can be roughly fitted by the formula

$$\frac{\nu_e}{U_0 \ell} \approx 1.86 (1 - n)^{2.06}, \quad (2.25)$$

where the range of porosity, $n = 1 - \pi(d/2\ell)^2$, of the available data is $0.945 \leq n \leq 0.994$. Estimating U_0 by the maximum orbital velocity in open water, $U_0 = \sqrt{gh_0}A/h_0$, we get

$$\sigma \approx 1.86 (1 - n)^{2.06} \frac{1}{k_0 \ell} \frac{A}{h_0}. \quad (2.26)$$

We point out that the data in Nepf (1999) are for random arrays of vegetation or cylinders. In the absence of empirical data from wave experiments for a periodic array of cylinders, the preceding empirical relation will be adopted in our numerical simulations.

Bed friction for waves is often modelled by a formula quadratic in the local velocity, but can be replaced by a linear law with the equivalent friction coefficient (Mei 1983; Nielsen 1992),

$$f = f_w \frac{4}{3\pi} \frac{U_0}{h_0}, \quad (2.27)$$

where f_w is a dimensionless friction factor in the quadratic law. Values of f_w can be estimated by an empirical formula of Swart (1974):

$$f_w = \exp [5.213\kappa^{0.194} - 5.977], \quad (2.28)$$

where $\kappa = r/A$ with r being the bed roughness (see Nielsen 1992). Consequently, by using $U_0 = \sqrt{gh_0}A/h_0$ we obtain

$$\alpha \approx 0.424 f_w \frac{1}{k_0 h_0} \frac{A}{h_0}. \quad (2.29)$$

h_0 (m)	ℓ (m)	n	$2\pi/\omega$ (min)	A/h_0	$1/k_0$ (m)	$k_0\ell$	k_0h_0	Max Re_d	σ	α
2.5	1	0.80	0.167	0.05	7.88	0.1269	0.317	1.25×10^5	0.027	0.003
2.5	1	0.85	1	0.05	47.29	0.0211	0.053	1.08×10^5	0.088	0.018
5.0	1	0.90	2	0.10	133.76	0.0075	0.037	2.50×10^5	0.217	0.051
5.0	2	0.90	10	0.05	688.79	0.0030	0.007	2.50×10^5	0.271	0.128
7.5	2	0.92	30	0.05	2460	0.0008	0.003	2.74×10^5	0.628	0.313

TABLE 1. Estimations of sample parameters. In all examples, $f_w = 0.045$ and values of σ and α are calculated according to (2.26) and (2.29), respectively.

It is known that $f_w = O(10^{-2})$ for $0 \leq \kappa \leq 0.1$. In later computations we shall take for illustration $f_w = 0.045$ corresponding to $\kappa = 0.05$.

Note that both σ and α depend on the wave amplitude, indicating the fact that turbulence and bed friction are inherently nonlinear, here represented by linear formulae. It is obvious that effects of coastal vegetation are more significant in stronger and longer waves as can be seen from (2.26) and (2.29). To provide some quantitative idea, σ and α are estimated in table 1 for several different incident wave conditions and micro-scale geometry. Their values are clearly larger for storm surges and tsunamis. Also, the maximum Reynolds numbers of these field examples are seen to be very much greater than those in the steady-flow data of Nepf (1999). Nevertheless we shall use (2.25) in later numerical simulations of laboratory experiments for relatively lower Reynolds numbers, in order to assess the applicability of steady-flow data to long waves. Good agreement would support the use of field-scale data of steady flows for long waves.

From here on only the dimensionless equations of depth averages will be used. For brevity, overbars and asterisks will be omitted.

3. Macro theory for sinusoidal waves

We first investigate sinusoidal waves propagating through an emergent forest. The depth-averaged horizontal velocity and the free-surface displacement can be expressed as

$$u_i = \tilde{u}_i(\mathbf{x})e^{-it}, \quad \eta = \tilde{\eta}(\mathbf{x})e^{-it}, \quad (3.1)$$

where spatial factors are distinguished by tildes. Equations (2.18) and (2.21) become

$$-\epsilon i \tilde{\eta} + \frac{\partial}{\partial x_i} (\tilde{u}_i h) = 0, \quad (3.2)$$

and

$$-\epsilon i \tilde{u}_i = -\frac{\partial \tilde{\eta}}{\partial x_i} + \epsilon \left(\sigma \frac{\partial^2 \tilde{u}_i}{\partial x_j \partial x_j} - \alpha \tilde{u}_i \right), \quad (3.3)$$

respectively.

3.1. Homogenization

The procedure employed here is similar to that for monochromatic sound waves through a periodic porous medium. In addition to the dimensionless coordinates \mathbf{x} which describe the micro-scale motion, we introduce the macro-scale

coordinates $\mathbf{x}' = \epsilon \mathbf{x}$ to describe the wave motion. The forest region is divided into periodic cells surrounding one or more cylinders. Two-scale expansions are then assumed for the dynamic unknowns:

$$\tilde{u}_i = \tilde{u}_i^{(0)} + \epsilon \tilde{u}_i^{(1)} + \epsilon^2 \tilde{u}_i^{(2)} + \dots, \quad \tilde{\eta} = \tilde{\eta}^{(0)} + \epsilon \tilde{\eta}^{(1)} + \epsilon^2 \tilde{\eta}^{(2)} + \dots, \quad (3.4)$$

where $\tilde{u}_i^{(n)} = \tilde{u}_i^{(n)}(\mathbf{x}, \mathbf{x}')$ and $\tilde{\eta}^{(n)} = \tilde{\eta}^{(n)}(\mathbf{x}, \mathbf{x}')$. The sea depth is assumed to depend on \mathbf{x}' only, i.e. $h = h(\mathbf{x}')$. The perturbation analysis is very similar to that for steady seepage flow (Ene & Sanchez-Palencia 1975; Keller 1980) and sound (Auriault 1980; Mei & Vernescu 2010) through a periodic porous medium. The key result is that at the leading order $\tilde{\eta}^{(0)}$ is independent of micro-scale coordinates. To determine its macro-scale behaviour one has to solve first for the tensor \tilde{K}_{ij} from the following micro-scale boundary-value problem in a unit cell:

$$\frac{\partial \tilde{K}_{ij}}{\partial x_i} = 0, \quad \mathbf{x} \in \Omega_f, \quad (3.5)$$

and

$$\sigma \frac{\partial^2 \tilde{K}_{ij}}{\partial x_k \partial x_k} + (i - \alpha) \tilde{K}_{ij} = \frac{\partial \tilde{A}_j}{\partial x_i} - \delta_{ij}, \quad \mathbf{x} \in \Omega_f, \quad (3.6)$$

where Ω_f denotes the fluid part in the unit cell of area Ω , and δ_{ij} is the Kronecker delta. On the cylinder walls, S_B , there must be no slip,

$$\tilde{K}_{ij} = 0, \quad \mathbf{x} \in S_B. \quad (3.7)$$

In addition, \tilde{K}_{ij} and \tilde{A}_j must be periodic from cell to cell. For uniqueness, the average of \tilde{A}_j over the cell volume Ω is set to zero,

$$\langle \tilde{A}_j \rangle = 0, \quad (3.8)$$

where

$$\langle Q \rangle = \frac{1}{\Omega} \iint_{\Omega_f} Q \, d\Omega \quad (3.9)$$

denotes the cell average. Then the seepage velocity is related to the macro-scale surface slope by

$$\langle \tilde{u}_i^{(0)} \rangle = -\langle \tilde{K}_{ij} \rangle \frac{\partial \tilde{\eta}^{(0)}(\mathbf{x}')}{\partial x'_j}, \quad (3.10)$$

which is an extension of Darcy's law, where $\langle \tilde{K}_{ij} \rangle$ is the hydraulic conductivity tensor defined as the cell average of \tilde{K}_{ij} . By taking the cell average of the mass conservation law at $O(\epsilon)$ and invoking Gauss' theorem and periodicity, we obtain

$$-i \tilde{\eta}^{(0)} + \frac{\partial (\langle \tilde{u}_j^{(0)} \rangle h)}{\partial x'_j} = 0. \quad (3.11)$$

Equations (3.10) and (3.11) can be combined to give an equation for the cell-averaged amplitude of the free-surface displacement,

$$i \tilde{\eta}^{(0)} + \langle \tilde{K}_{ij} \rangle \frac{\partial}{\partial x'_i} \left(h \frac{\partial \tilde{\eta}^{(0)}}{\partial x'_j} \right) = 0. \quad (3.12)$$

We note that the dimensionless hydraulic conductivity tensor $\langle \tilde{K}_{ij} \rangle$ is related to its dimensional counterpart $\langle \tilde{K}_{ij}^{phy} \rangle$ by $\langle \tilde{K}_{ij} \rangle = \langle \tilde{K}_{ij}^{phy} \rangle k_0 h_0 / \sqrt{g h_0}$, and depends on the wave frequency through σ and α . Note also that \tilde{A}_i and \tilde{K}_{ij} are independent of the local sea depth, therefore $\langle \tilde{K}_{ij} \rangle$ is the same for all \mathbf{x}' . In the absence of forests and bottom friction, (3.6) gives $\tilde{K}_{ij} \rightarrow i\delta_{ij}$. Consequently, (3.10) and (3.12) reduce to the standard linearized equations governing inviscid shallow water waves.

3.2. Numerical solution of the micro-scale cell problem

The micro-scale problem, (3.5)–(3.8), is similar to that for sound through a periodic porous medium (Auriault 1980; Sheng & Zhou 1988; Zhou & Sheng 1989) and can be solved by the Galerkin finite element method. For this purpose the governing equations are first rewritten in the weak form as

$$\iint_{\Omega} \sum_{i=1}^2 \frac{\partial \tilde{K}_{ij}}{\partial x_i} \varphi_j d\Omega = 0, \quad (3.13)$$

and

$$\iint_{\Omega} \left\{ \left[(i - \alpha) \tilde{K}_{ij} - \frac{\partial \tilde{A}_j}{\partial x_i} + \delta_{ij} \right] \phi_{ij} + \sigma \nabla \tilde{K}_{ij} \cdot \nabla \phi_{ij} \right\} d\Omega = \sigma \oint_{S_B} \frac{\partial \tilde{K}_{ij}}{\partial n_{S_B}} \phi_{ij} ds, \quad (3.14)$$

where φ_j and ϕ_{ij} are the weighting functions and n_{S_B} is the unit normal to the cylinder wall S_B . No summation is taken over repeated indices j in (3.13) and i and j in (3.14). Use has been made of Gauss' theorem in obtaining (3.14). After discretizing the fluid region in the unit cell into triangular elements, the unknown variables \tilde{K}_{ij} and \tilde{A}_j are represented by linear interpolation functions which are also used for the weighting functions φ_j and ϕ_{ij} . Then, the integral conditions above are transformed into algebraic equations for the unknown coefficients at each node, which are solved numerically. For a circular cylinder inside a unit square cell, figure 1 shows the discretization and the spatial variation of \tilde{K}_{11} inside a cell for $n = 0.85$, $\sigma = 0.088$ and $\alpha = 0.018$ which correspond to the second row in table 1. Due to cellular symmetry, $\langle \tilde{K}_{ij} \rangle \equiv \mathcal{K} \delta_{ij}$ is isotropic. Figure 2 shows the magnitude $|\mathcal{K}|$ and phase θ of the normalized hydraulic conductivity against the wave frequency parameter, $k_0 h_0$, for $n = 0.8, 0.85, 0.9$, $h_0 = 2.5$ m, $\ell = 1$ m, $A/h_0 = 0.05$, and $f_w = 0.045$. Both quantities start from zero at $k_0 h_0 = 0$ (steady flow) and increase linearly at first with $k_0 h_0$ (or with frequency). Because of the normalization the dimensional hydraulic conductivity is $\mathcal{K}^{phy} = \mathcal{K} \sqrt{g h_0} / k_0 h_0$. The steady-flow limit of \mathcal{K}^{phy} is proportional to the local slope of \mathcal{K} , i.e. $(d\mathcal{K}/d(k_0 h_0)) \sqrt{g h_0}$ at the origin ($k_0 h_0 = 0$) and is finite and real. Figure 2 also reveals that for a given incident wave both $|\mathcal{K}|$ and θ are larger for a smaller tree trunk, i.e. a higher porosity n . Figure 3 shows the dependence on σ . Since $\sigma \propto 1/\omega \ell^2$, both $|\mathcal{K}|$ and θ decrease monotonically with increasing σ . Also since $\alpha \propto 1/\omega$, their dependence on α is similar, and is not plotted.

We now turn to the macro-scale problems.

3.3. Constant water depth

For analytical simplicity, we consider first problems in one horizontal dimension with uniform water depth everywhere, i.e. $h = 1$. The input parameters correspond to those shown in figure 2, representative of weak monochromatic waves.

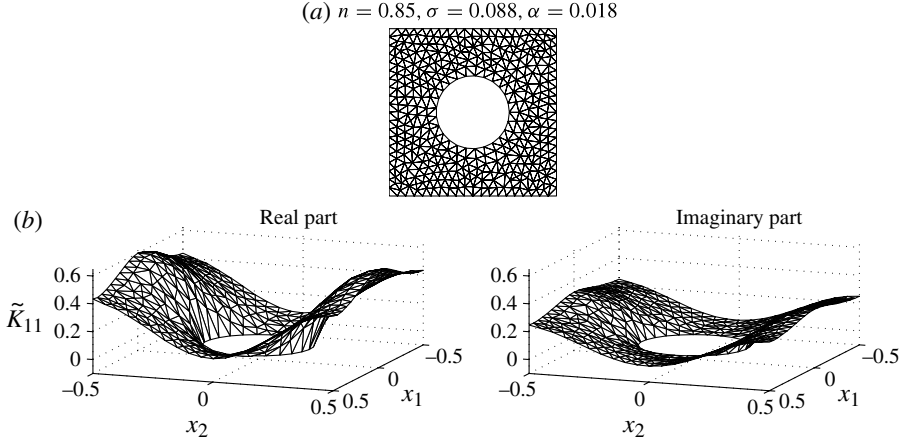


FIGURE 1. (a) Discretization of a typical unit cell with a circular cylinder inside a square. (b) Spatial distributions, $\tilde{K}_{11}(\mathbf{x})$. Due to isotropy, only \tilde{K}_{11} is needed. The input parameters are listed in the second row of table 1.

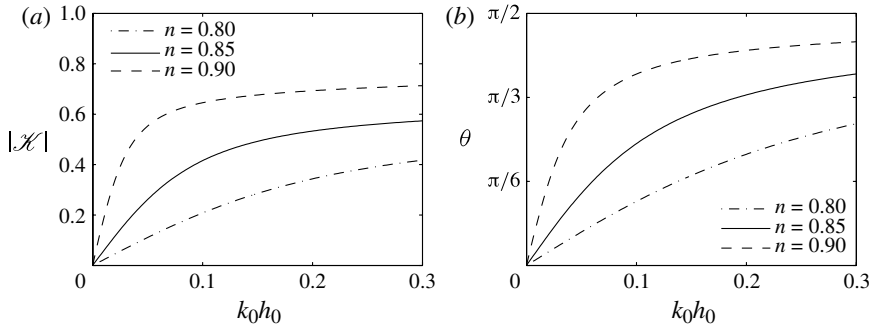


FIGURE 2. Complex hydraulic conductivity, $\mathcal{K} = |\mathcal{K}|e^{i\theta}$, as a function of depth-to-wavelength ratio, $k_0 h_0$: (a) magnitude $|\mathcal{K}|$, (b) phase θ . The cell geometry is a circular cylinder inside a square with $n = 0.8, 0.85, 0.9$. In all cases, $h_0 = 2.5$ m, $\ell = 1$ m, $A/h_0 = 0.05$ and $f_w = 0.045$ are fixed. The values of σ and α are calculated from (2.26) and (2.29) for given n and $k_0 h_0$.

3.3.1. Very thick forest

Let the forest occupy the semi-infinite domain, $0 < x' < \infty$. Inside the forest, we obtain from (3.12)

$$\frac{\partial^2 \tilde{\eta}^{(0)}}{\partial x'^2} + \frac{i}{\mathcal{K}} \tilde{\eta}^{(0)} = 0, \quad x' > 0, \quad (3.15)$$

where $\mathcal{K} = \mathcal{K}^R + i\mathcal{K}^I$ is the hydraulic conductivity. The solution is

$$\tilde{\eta}^{(0)} = B e^{-x'/a}, \quad x' > 0, \quad (3.16)$$

with

$$a = \sqrt{i\mathcal{K}} = a^R + ia^I = \sqrt{|\mathcal{K}|} e^{i((\theta/2) + (\pi/4))}, \quad \theta = \tan^{-1} \frac{\mathcal{K}^I}{\mathcal{K}^R} < \frac{\pi}{2}. \quad (3.17)$$

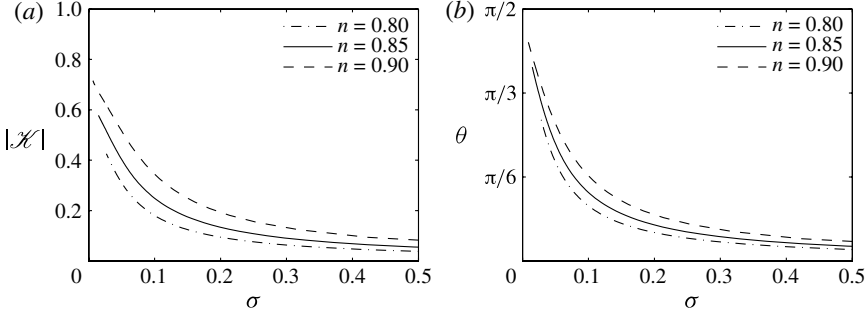


FIGURE 3. Dependence of the complex hydraulic conductivity \mathcal{K} on the controlling parameter σ : (a) magnitude $|\mathcal{K}|$, (b) phase θ . In all cases presented here, $\alpha = 0$.

The corresponding velocity can be obtained from (3.10) as

$$\langle \tilde{u}^{(0)} \rangle = \frac{1}{a} \mathcal{K} B e^{-x'/a}, \quad x' > 0. \quad (3.18)$$

Equations (3.16) and (3.18) represent a propagating wave with decreasing amplitude.

We now consider the open water, $x' < 0$, where dissipation is neglected. Solutions for a frictionless seabed can be expressed as

$$\tilde{\eta} = e^{ix'} + R e^{-ix'}, \quad \tilde{u} = e^{ix'} - R e^{-ix'}, \quad x' < 0. \quad (3.19)$$

Matching at $x' = 0$ of the surface displacement and horizontal velocity yields two algebraic equations for R and B , with the solutions

$$R = \frac{a - \mathcal{K}}{a + \mathcal{K}} \quad \text{and} \quad B = \frac{2a}{a + \mathcal{K}}, \quad (3.20)$$

where R denotes the reflection coefficient. It can be readily shown that

$$|R|^2 = \frac{(a^R - \mathcal{K}^R)^2 + (a^I - \mathcal{K}^I)^2}{(a^R + \mathcal{K}^R)^2 + (a^I + \mathcal{K}^I)^2} \leq 1, \quad (3.21)$$

and

$$|B|^2 = \frac{4|a|^2}{(a^R + \mathcal{K}^R)^2 + (a^I + \mathcal{K}^I)^2} \geq 0. \quad (3.22)$$

Clearly waves are damped out after a distance of $x' = O(\sqrt{|\mathcal{K}|})$.

Using the numerical values of \mathcal{K} in figure 2, we show in figure 4 the square of the reflection coefficient, $|R|^2$, and the free-surface elevations inside the forest for different porosities and dimensionless frequency. It is evident that reflection increases with the wave period (or wavelength) and decreases with larger porosity. Since by normalization the physical distance is x'/k_0 , the wave amplitude is more rapidly attenuated for longer waves, as shown in figure 4(b).

3.3.2. A finite forest belt

Consider next a finite forest belt, $0 < x' < L'_B$, where $L'_B = k_0 L_B$ is the ratio of forest thickness (L_B) to typical wavelength ($1/k_0$). In the region of incidence, $x' < 0$, (3.19) still holds. Behind the forest, $x' > L'_B$, the solutions can be expressed as

$$\tilde{\eta} = \tilde{u} = T e^{ix'}, \quad x' > L'_B. \quad (3.23)$$

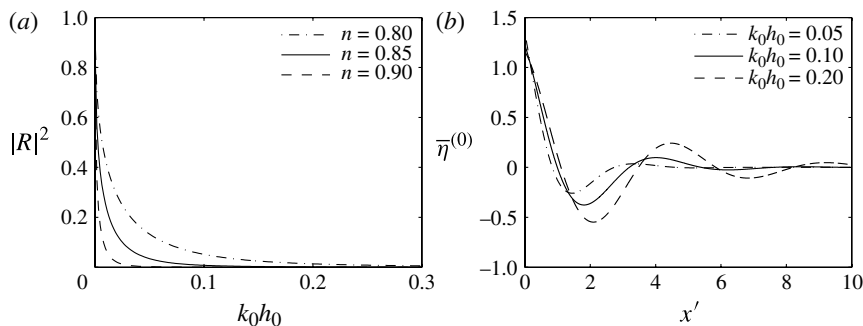


FIGURE 4. Periodic waves propagating through a semi-infinite forest in a constant water depth region: (a) the square of the reflection coefficient, $|R|^2$, against the wave frequency parameter, $k_0 h_0$, for $n = 0.8, 0.85, 0.9$; (b) snapshots of free-surface elevation at the phase $t = 0$ for the case of $n = 0.85$. As can be seen, $|R|^2$ grows with increasing wavelength (i.e. smaller $k_0 h_0$). In all calculations, the input parameters are same as in figure 2.

Inside the forests, $0 < x' < L'_B$, the solution is now of the form

$$\tilde{\eta}^{(0)} = B e^{-x'/a} + D e^{x'/a}. \quad (3.24)$$

Matching the displacement and velocity at both $x' = 0$ and $x' = L'_B$, we obtain

$$R = \frac{(a^2 - \mathcal{K}^2)(-1 + e^{2L'_B/a})}{(a + \mathcal{K})^2 e^{2L'_B/a} - (a - \mathcal{K})^2}, \quad (3.25a)$$

$$B = \frac{2a(a + \mathcal{K})e^{2L'_B/a}}{(a + \mathcal{K})^2 e^{2L'_B/a} - (a - \mathcal{K})^2}, \quad (3.25b)$$

$$D = \frac{-2a(a - \mathcal{K})}{(a + \mathcal{K})^2 e^{2L'_B/a} - (a - \mathcal{K})^2}, \quad (3.25c)$$

$$T = \frac{4a\mathcal{K}e^{L'_B(1/a-i)}}{(a + \mathcal{K})^2 e^{2L'_B/a} - (a - \mathcal{K})^2}. \quad (3.25d)$$

Taking $L'_B \rightarrow \infty$, coefficients R and B reduce to those shown in (3.20). Again for the cell with a single cylinder at the centre, the effects of different forest thickness and porosity are shown in figure 5. Values of σ and α are calculated from (2.26) and (2.29) respectively for $n = 0.8, 0.85, 0.9$ with all other parameters listed in the second row of table 1. The reflection coefficient, $|R|$, does not vary monotonically with respect to the dimensionless forest thickness, L'_B . This is a characteristic well-known in one-dimensional scattering, as the multiply reflected waves from the opposite ends can have different phases depending on their travel distances and interfere with one another either constructively or destructively (Mei 1983). As $L'_B \rightarrow \infty$, R reaches asymptotically the value for the semi-infinite forest given in the previous section and indicated by triangles in figure 5. Spatial decay of the surface waves is more rapid for greater dimensionless $L'_B = k_0 L_B$, i.e. thicker forest relative to the wavelength.

3.4. Variable water depth

In this section, we consider the effects of varying water depth where h varies linearly in x' over some distance. For validation, the analytical solutions have been checked by discrete numerical computations.

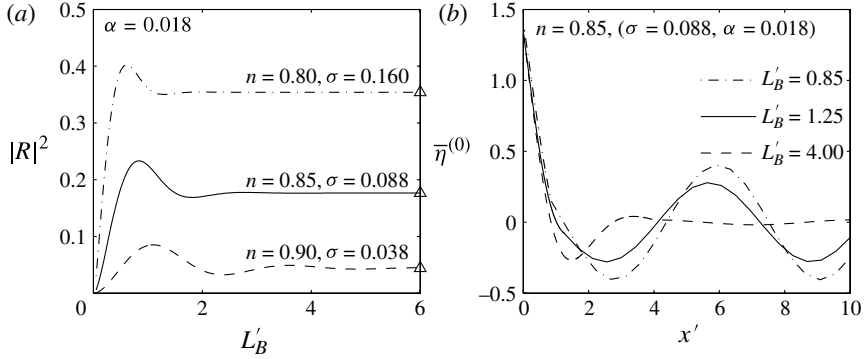


FIGURE 5. Periodic waves propagating through a finite patch of forest in a constant water depth: (a) the square of reflection coefficient, $|R|^2$, against the dimensionless thickness of forest, L'_B ; (b) snapshots of free-surface elevation at $t = 0$ for $n = 0.85$ and $L'_B = 0.85, 1.25, 4$. Lines are the results from (3.24) and (3.25) while triangles give $|R|^2$ of $L'_B \rightarrow \infty$ predicted by (3.21). In all calculations, $k_0 \ell_0 = 0.0211$ and $k_0 h_0 = 0.053$, corresponding to the second row of table 1.

3.4.1. Forest on a plane beach

Let the open water be of constant depth: $h = 1$, $x' < 0$. A forest covers the entire beach of a constant slope S , i.e. $h = 1 - Sx'$ in $0 < x' < 1/S$. Over the sloping bottom, the mean wave equation, (3.12), becomes

$$i\tilde{\eta}^{(0)} - S\mathcal{K} \frac{\partial \tilde{\eta}^{(0)}}{\partial x'} + (1 - Sx')\mathcal{K} \frac{\partial^2 \tilde{\eta}^{(0)}}{\partial x'^2} = 0. \quad (3.26)$$

Assuming perfect reflection at the shore, $x' = 1/S$, the solution on the beach can be expressed as

$$\tilde{\eta}^{(0)} = \frac{B}{\sqrt{S}} J_0 \left(\frac{2i}{Sa} \sqrt{1 - Sx'} \right), \quad (3.27)$$

where $J_n(z)$ is the Bessel function of the first kind. Again, the matching conditions at $x' = 0$ require

$$1 + R = \frac{B}{\sqrt{S}} J_0 \left(\frac{2i}{Sa} \right), \quad 1 - R = -\frac{B}{\sqrt{S}} \sqrt{a} J_1 \left(\frac{2i}{Sa} \right). \quad (3.28)$$

Solving the above algebraic equations, we obtain

$$R = \frac{J_0 \left(\frac{2i}{Sa} \right) + aJ_1 \left(\frac{2i}{Sa} \right)}{J_0 \left(\frac{2i}{Sa} \right) - aJ_1 \left(\frac{2i}{Sa} \right)} \quad \text{and} \quad B = \frac{2\sqrt{S}}{J_0 \left(\frac{2i}{Sa} \right) - aJ_1 \left(\frac{2i}{Sa} \right)}. \quad (3.29)$$

As a check, we take the limit of no forest, then $\mathcal{K} \rightarrow i$ and the reflection coefficient becomes

$$R \rightarrow \frac{J_0(2/S) + iJ_1(2/S)}{J_0(2/S) - iJ_1(2/S)}, \quad (3.30)$$

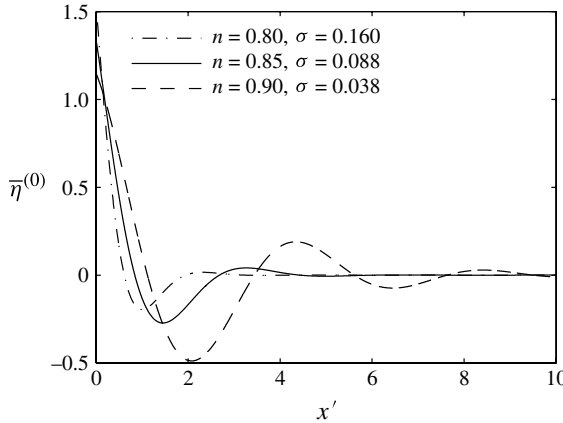


FIGURE 6. Snapshots at $t = 0$ of periodic waves propagating through a forest on a plane beach of slope $S = 1/20$. Porosities are: $n = 0.8, 0.85, 0.9$ and $k_0 h_0 = 0.053$. Other parameters are shown in the second row of table 1. The corresponding hydraulic conductivity, \mathcal{K} , is shown in figure 2.

and the coefficient B reduces to

$$B \rightarrow \frac{2\sqrt{S}}{J_0(2/S) - iJ_1(2/S)}. \quad (3.31)$$

For very small bottom slope $S \ll 1$, (3.30) and (3.31) reduce to the solutions of Keller & Keller (1964). Figure 6 plots the free-surface elevation inside forests for different values of n . The behaviour of these examples is similar to that of constant water depth cases.

3.4.2. A finite forest belt on a sloping step

Let the sea bed be a plane slope in the middle region and horizontal on both sides, i.e.

$$h = \begin{cases} 1, & x' < 0 \\ 1 - Sx', & 0 < x' < L'_B \\ 1 - SL'_B, & x' > L'_B. \end{cases} \quad (3.32)$$

The forest covers the sloping part only. Now, the solution on the slope becomes

$$\tilde{\eta}^{(0)} = \frac{1}{\sqrt{S}} \left\{ BI_0 \left(\frac{2a}{S} \sqrt{1 - Sx'} \right) + DK_0 \left(\frac{2a}{S} \sqrt{1 - Sx'} \right) \right\}, \quad 0 < x' < L'_B, \quad (3.33)$$

where $I_n(z)$ and $K_n(z)$ are the modified Bessel function of the first kind and second kind, respectively. Coefficients B and D are yet to be determined. Let the transmitted wave in the open water $x' > L'_B$ be

$$\tilde{\eta} = Te^{imx'}, \quad \tilde{u} = mTe^{imx'} \quad \text{with} \quad m = \frac{1}{\sqrt{h_B}} = \frac{1}{\sqrt{1 - SL'_B}}, \quad (3.34)$$

while the free-surface elevation and horizontal velocity in the incident wave region, $x' < 0$, are given by (3.19). By matching at both $x' = 0$ and $x' = L'_B$, the unknown

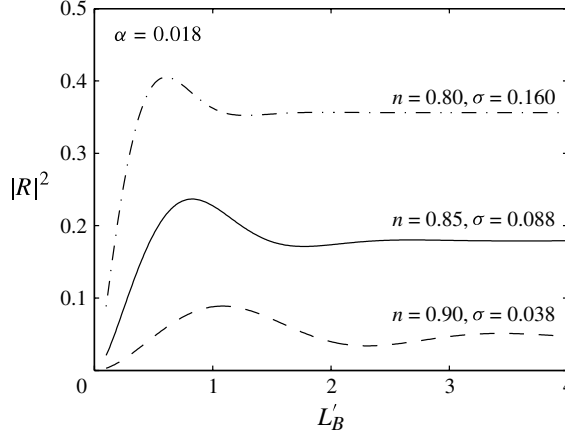


FIGURE 7. Square of the reflection coefficient, $|R|^2$, for waves through a finite forest belt of dimensionless thickness L'_B on a sloping step with a constant slope $s = 1/20$. Parameters used in all calculations are same as those shown in figure 6.

coefficients can be found as

$$R = \frac{c_{34} [(c_{13} - c_{23})c_{42} - (c_{12} - c_{22})c_{43}] - c_{44} [(c_{13} - c_{23})c_{32} - (c_{12} - c_{22})c_{33}]}{c_{34} [(c_{13} + c_{23})c_{42} - (c_{12} + c_{22})c_{43}] - c_{44} [(c_{13} + c_{23})c_{32} - (c_{12} + c_{22})c_{33}]}, \quad (3.35a)$$

$$B = \frac{2(c_{33}c_{44} - c_{34}c_{43})}{c_{34} [(c_{13} + c_{23})c_{42} - (c_{12} + c_{22})c_{43}] - c_{44} [(c_{13} + c_{23})c_{32} - (c_{12} + c_{22})c_{33}]}, \quad (3.35b)$$

$$D = \frac{2(c_{32}c_{44} - c_{34}c_{42})}{(c_{12} + c_{22})(c_{33}c_{44} - c_{34}c_{43}) - (c_{13} + c_{23})(c_{32}c_{44} - c_{34}c_{42})}, \quad (3.35c)$$

$$T = \frac{-2(c_{32}c_{43} - c_{33}c_{42})}{c_{34} [(c_{13} + c_{23})c_{42} - (c_{12} + c_{22})c_{43}] - c_{44} [(c_{13} + c_{23})c_{32} - (c_{12} + c_{22})c_{33}]}, \quad (3.35d)$$

where

$$c_{12} = \frac{1}{\sqrt{S}} I_0(Z), \quad c_{13} = \frac{1}{\sqrt{S}} K_0(Z), \quad (3.36a)$$

$$c_{22} = -\frac{2i}{S\sqrt{S}} \frac{1}{Z} I_1(Z), \quad c_{23} = \frac{2i}{S\sqrt{S}} \frac{1}{Z} K_1(Z), \quad (3.36b)$$

$$c_{32} = \frac{1}{\sqrt{S}} I_0(Z\sqrt{h_B}), \quad c_{33} = \frac{1}{\sqrt{S}} K_0(Z\sqrt{h_B}), \quad (3.36c)$$

$$c_{42} = -\frac{2i}{S\sqrt{S}} \frac{1}{Z\sqrt{h_B}} I_1(Z\sqrt{h_B}), \quad c_{43} = \frac{2i}{S\sqrt{S}} \frac{1}{Z\sqrt{h_B}} K_1(Z\sqrt{h_B}), \quad (3.36d)$$

$$c_{34} = \exp(imL'_B), \quad c_{44} = m \exp(imL'_B), \quad (3.36e)$$

with $Z = 2/(Sa)$. Recall that a and m are given in (3.17) and (3.34), respectively.

In figure 7, the square of reflection coefficient, $|R|^2$, is displayed against the dimensionless thickness of the forest, L'_B . Again, $|R|^2$ does not vary monotonically with L'_B as discussed in § 3.3.2. The features are qualitatively similar to those for a horizontal seabed.

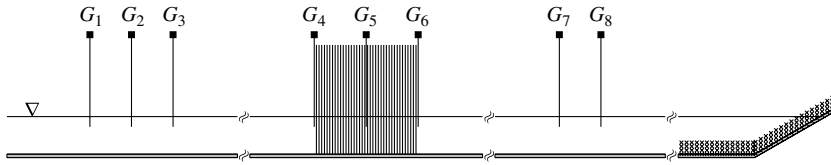


FIGURE 8. Sketch of experimental setup with sample arrangement of wave gauges G_i (not to scale). The model forest has a width of 0.54 m and a thickness of 1.08 m. Wave flume is 0.54 m wide and 0.6 m deep. The length of the constant depth part is 25 m. Gauge locations for different incident waves are listed in table 2.

Wave type	G_1	G_2	G_3	G_4	G_5	G_6	G_7	G_8
Periodic waves	-3.085	-2.935	-2.685	-0.005	0.540	1.085	2.025	2.275
Wave packets	-	-	-3.025	-0.100	0.715	-	2.260	2.660
Solitary waves	-	-3.205	-3.005	-0.005	0.540	1.085	1.385	-

TABLE 2. Positions of wave gauges (in metres) (see figure 8). The origin is set at the front edge of the model forest. In some tests records were not taken from all gauges.

3.5. Experiments and numerical simulation for periodic waves

A series of laboratory experiments has been conducted in the glass-walled wave flume (32 m long, 0.54 m wide, and 0.6 m deep) in the Hydraulics Laboratory at the Nanyang Technological University, Singapore. At one end, the flume is equipped with a piston-type wavemaker which has active wave absorbing capability. At the other end, there is an energy absorbing beach of 1-to-7 slope to minimize the reflection. In the centre region of constant water depth, Perspex cylinders of 1 cm diameter were installed as a square array spanning the entire width of the flume. The model forest has a total thickness of 1.08 m and a porosity $n = 0.913$. Several resistance-type wave gauges were employed to record time histories of free-surface elevation at a sampling rate of 100 Hz. The experimental setup is sketched in figure 8. Three types of incident waves were studied: periodic waves, transient wave packets, and solitary waves. The maximum Reynolds numbers in the experiments are in a moderate range of 200–2500 which is similar to that of Nepf (1999) ($400 < Re_d < 2000$) for steady flows.

Conditions for the first set of tests, all for $h_0 = 12$ cm, are listed in table 3. A broad range of wave periods including relatively short waves were tested. To minimize the effect of nonlinearity, the amplitude of the longer waves (periods = 2.0, 2.5, 3.0 s) is kept very small. The coefficient of beach reflection $|R_B|$ in the absence of the forest is quite large for the three longest periods (2.0, 2.5, 3.0 s) and relatively small for short waves due to partial breaking. In our numerical simulations the controlling parameter σ is estimated by (2.26) which varies with the different input amplitudes for different frequencies, hence the predictions do not fall on a smooth curve. Since the tank bottom is smooth, we take $\alpha = 0$. For the longest waves, higher harmonics are noticeable. For instance, the Stokes–Ursell parameter for the test case with period = 3.0 s is $A/k_0^2 h_0^3 \approx 0.38$, which is not small. The experimental reflection and transmission coefficients are extracted from the data by taking only the first harmonics. Initial comparison of predictions with data showed reasonable agreement only for relatively short waves, but a large discrepancy for the reflection coefficients of the three longest waves. We attribute the discrepancy to beach reflection and nonlinearity.

Period (s)	h_0 (m)	$2A$ (m)	$1/k_0$ (m)	$k_0 h_0$	$k_0 L_B$	Max Re_d	σ	$ R_B $
0.8	0.12	0.0232	0.1207	0.9940	8.9464	1049	0.0047	0.065
1.0	0.12	0.0253	0.1587	0.7560	6.8044	1144	0.0068	0.101
1.2	0.12	0.0272	0.1956	0.6135	5.5218	1230	0.0090	0.050
1.4	0.12	0.0246	0.2318	0.5177	4.6593	1112	0.0096	0.014
1.6	0.12	0.0239	0.2676	0.4485	4.0362	1081	0.0108	0.022
1.8	0.12	0.0243	0.3031	0.3959	3.5633	1099	0.0124	0.099
1.9	0.12	0.0243	0.3208	0.3741	3.3670	1099	0.0132	0.090
2.0	0.12	0.0068	0.3384	0.3546	3.1915	307	0.0039	0.178
2.5	0.12	0.0065	0.4261	0.2816	2.5344	294	0.0047	0.239
3.0	0.12	0.0050	0.5134	0.2337	2.1036	226	0.0043	0.250

TABLE 3. Experimental conditions for periodic waves through a coastal forest. In all cases, the forest thickness is $L_B = 1.08$ m and porosity $n = 0.913$. Controlling parameter σ is estimated by (2.26). $|R_B|$ is the measured beach reflection coefficient without the forest. See figure 9 for corresponding reflection and transmission coefficients.

As a partial correction we adjusted the experimental results from the measured data by accounting for the one-time passage of a beach-reflected wave as follows:

$$|R'| = |R| + |T| \times |R_B| \times |T|, \quad |T'| = |T| - |T| \times |R_B| \times |R|, \quad (3.37)$$

where $|R'|$ and $|T'|$ are determined directly from the first harmonics of the data. From these equations the adjusted values $|R|$ and $|T|$ are calculated. Of course the above correction is only a crude estimate without proper account of the wave phases and wave nonlinearity. In figure 9 we compare both the measured and the adjusted data with the predictions without a beach, shown by crosses. The agreement is much improved. The quantity $1 - |R|^2 - |T|^2$ which measures the percentage of wave energy dissipated by the model forest is also shown. Note that although the parameters σ and α are larger for longer waves, the ratio $L'_B = k_0 L_B$ is smaller since $L_B = 1.08$ m is fixed. This leads to weaker attenuation hence higher transmission for longer waves, as shown in figure 9. To bypass the complications of beach reflection and nonlinearity unavoidable in laboratory tests on periodic long waves, we shall test our theory for transient long waves of finite duration to be presented later in § 4.5.

We have conducted additional tests for shorter waves in deeper water and a wide range of wave amplitudes under conditions listed in table 4. For three wave periods (Set A: 0.8; Set B: 1; Set C: 1.2 (s)) and two water depths (0.15, 0.2 m), the wave amplitudes ranged from 1 to 4 cm. Figure 10 shows the corresponding predictions of reflection and transmission coefficients and the degree of dissipation, $1 - |R|^2 - |T|^2$, by (3.25) along with measured data. Again, the agreement is surprisingly good even for weakly nonlinear waves of intermediate length. Extension of the present theory to $k_0 h_0 = O(1)$ would of course be desirable for a more valid comparison.

4. Macro theory for transient waves

4.1. Homogenization

Of interest in the protection against weak or distant tsunamis, let us consider a transient wave invading a forest. Again, assuming two-scale expansions of the dimensionless horizontal velocity and the free-surface elevation,

$$u_i = u_i^{(0)} + \epsilon u_i^{(1)} + \epsilon^2 u_i^{(2)} + \cdots, \quad \eta = \eta^{(0)} + \epsilon \eta^{(1)} + \epsilon^2 \eta^{(2)} + \cdots, \quad (4.1)$$

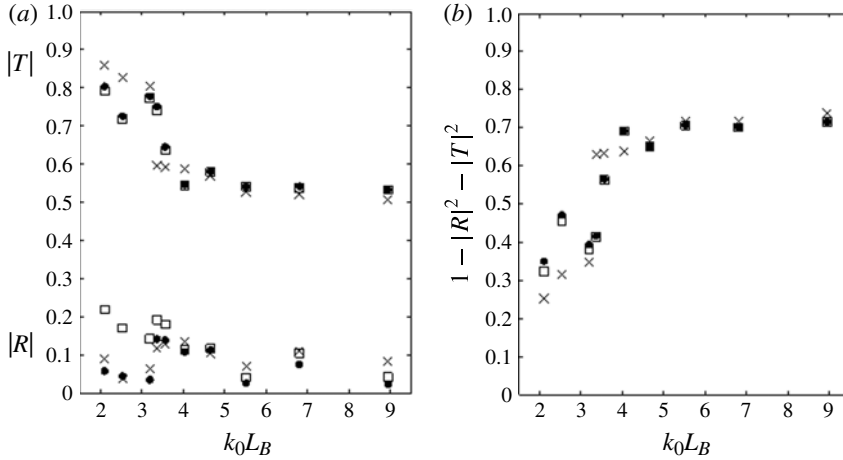


FIGURE 9. (a) Reflection coefficient ($|R|$) and transmission coefficient ($|T|$) as functions of $k_0 L_B$. (b) $1 - |R|^2 - |T|^2$ vs. $k_0 L_B$. Hollow squares: measured data; solid dots: adjusted data; crosses: predictions without the beach.

Set	Period (s)	h_0 (m)	$1/k_0$ (m)	$k_0 h_0$	$k_0 L_B$	$\sigma/(A/h_0)$	(Max Re_d)/(A/h ₀)
A	0.8	0.15	0.130	1.152	8.297	0.0528	12 130
		0.20	0.141	1.415	7.642	0.0573	14 007
B	1.0	0.15	0.174	0.864	6.223	0.0703	12 139
		0.20	0.193	1.037	5.597	0.0782	14 107
C	1.2	0.15	0.215	0.696	5.014	0.0873	12 131
		0.20	0.243	0.825	4.454	0.0983	14 107

TABLE 4. Experimental conditions for a wide range of A/h_0 shown in figure 10. Controlling parameter σ is estimated by (2.26). In all cases, the forest thickness is $L_B = 1.08$ m and porosity $n = 0.913$. The corresponding maximum Reynolds numbers are in the range of $490 < \text{Max } Re_d < 2520$. Note that σ and Re_d are proportional to A/h_0 by definition.

where $u^{(n)} = u^{(n)}(\mathbf{x}, \mathbf{x}', t)$ and $\eta^{(n)} = \eta^{(n)}(\mathbf{x}, \mathbf{x}', t)$, we obtain the perturbation equations. At $O(\epsilon^0)$:

$$\frac{\partial u_i^{(0)}}{\partial x_i} = 0, \quad (4.2)$$

$$\frac{\partial \eta^{(0)}}{\partial x_i} = 0. \quad (4.3)$$

Thus the leading-order free-surface height varies only over the macro-scale, $\eta^{(0)} = \eta^{(0)}(\mathbf{x}', t)$. At $O(\epsilon)$,

$$\frac{\partial \eta^{(0)}}{\partial t} + \frac{\partial (u_i^{(0)} h)}{\partial x'_i} + h \frac{\partial u_i^{(1)}}{\partial x_i} = 0, \quad (4.4)$$

$$\frac{\partial u_i^{(0)}}{\partial t} = -\frac{\partial \eta^{(0)}}{\partial x'_i} - \frac{\partial \eta^{(1)}}{\partial x_i} + \sigma \frac{\partial^2 u_i^{(0)}}{\partial x_j \partial x_j} - \alpha u_i^{(0)}. \quad (4.5)$$

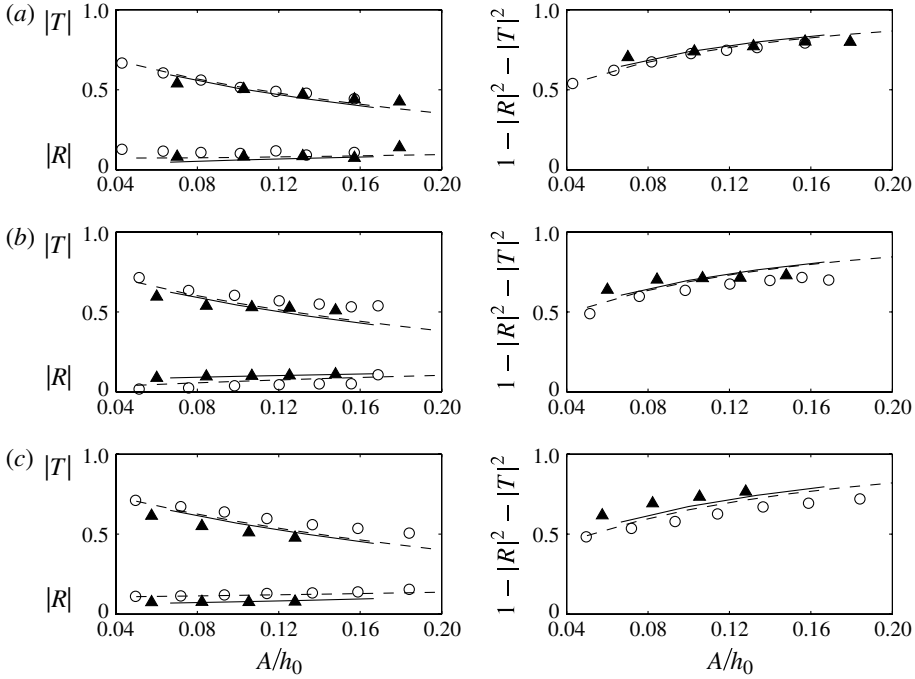


FIGURE 10. Reflection ($|R|$) and transmission ($|T|$) coefficients of periodic waves crossing a finite patch of forest in constant water depth, as functions of amplitude-to-depth ratio (A/h_0). Symbols show the measured data while lines show the predictions by (3.25). Triangles and solid lines are for $h_0 = 0.15$ m, while circles and dashed lines are for depth $h_0 = 0.2$ m. See table 4 for experimental conditions: (a) Set A, (b) Set B, (c) Set C.

The unknown $u^{(0)}$ and $\eta^{(1)}$ can be represented as convolution integrals

$$u_i^{(0)}(x_k, x'_k, t) = - \int_0^t K_{ij}(x_k, t - \tau) \frac{\partial \eta^{(0)}(x'_k, \tau)}{\partial x'_j} d\tau, \quad (4.6)$$

and

$$\eta^{(1)} = - \int_0^t A_j(x_k, t - \tau) \frac{\partial \eta^{(0)}(x'_k, \tau)}{\partial x'_j} d\tau. \quad (4.7)$$

It follows from (4.2) that

$$\frac{\partial K_{ij}}{\partial x_i} = 0, \quad \forall x_i \in \Omega, \quad (4.8)$$

on the micro-scale. Substituting (4.6) and (4.7) into (4.5) and employing the Leibniz rule, the left-hand side of (4.5) becomes

$$\frac{\partial u_i^{(0)}}{\partial t} = - \int_0^t \frac{\partial K_{ij}(x_k, t - \tau)}{\partial t} \frac{\partial \eta^{(0)}(x'_k, \tau)}{\partial x'_j} d\tau - K_{ij}(x_k, 0_+) \frac{\partial \eta^{(0)}(x'_k, t)}{\partial x'_j}. \quad (4.9)$$

The right-hand side of (4.5) can be expressed as

$$- \frac{\partial \eta^{(0)}}{\partial x'_i} - \int_0^t d\tau \frac{\partial \eta^{(0)}}{\partial x'_j} \left\{ - \frac{\partial A_j(x_k, t - \tau)}{\partial x_i} + \sigma \frac{\partial^2 K_{ij}(x_k, t - \tau)}{\partial x_k \partial x_k} - \alpha K_{ij} \right\}. \quad (4.10)$$

We now impose the initial condition,

$$K_{ij}(x_k, 0_+) = \delta_{ij}, \quad (4.11)$$

so that the last term in (4.9) can be written as $-\partial\eta^{(0)}/\partial x'_i$ which cancels the first term in (4.10). Finally, (4.5) becomes

$$\int_0^t d\tau \frac{\partial\eta^{(0)}}{\partial x'_i} \Big|_{\tau} \left\{ \frac{\partial K_{ij}}{\partial t} \right\}_{t-\tau} = \int_0^t d\tau \frac{\partial\eta^{(0)}}{\partial x'_i} \Big|_{\tau} \left\{ -\frac{\partial A_j}{\partial x_i} + \sigma \frac{\partial^2 K_{ij}}{\partial x_k \partial x_k} - \alpha K_{ij} \right\}_{t-\tau}. \quad (4.12)$$

Hence, K_{ij} is governed on the micro-scale by

$$\frac{\partial K_{ij}}{\partial t} = -\frac{\partial A_j}{\partial x_i} + \sigma \frac{\partial^2 K_{ij}}{\partial x_k \partial x_k} - \alpha K_{ij}, \quad \forall x_i \in \Omega, t > 0. \quad (4.13)$$

Again, K_{ij} and A_j must be Ω -periodic and satisfy

$$K_{ij} = 0, \quad x_k \in S_B, \quad (4.14)$$

and

$$\langle A_j \rangle = 0. \quad (4.15)$$

Defined by (4.8), (4.11) and (4.13)–(4.15), the initial-boundary-value problem in the unit cell can be solved numerically by the finite-element method. Note that these equations, hence their solution, are independent of the macro coordinates. Then, the cell-averaged horizontal velocity can be obtained as

$$\langle u_i^{(0)}(\mathbf{x}, \mathbf{x}', t) \rangle = - \int_0^t \langle K_{ij}(\mathbf{x}, t - \tau) \rangle \frac{\partial\eta^{(0)}(\mathbf{x}', \tau)}{\partial x'_j} d\tau, \quad (4.16)$$

which is the transient Darcy's law. By taking the cell average of (4.4) and invoking Gauss' theorem and Ω -periodicity, we obtain

$$\frac{\partial\eta^{(0)}}{\partial t} + \frac{\partial}{\partial x'_i} \left(\langle u_i^{(0)} \rangle h \right) = 0. \quad (4.17)$$

Combination of (4.17) with (4.16) leads to the mean-field equation for the free-surface displacement

$$\frac{\partial\eta^{(0)}}{\partial t} = \frac{\partial}{\partial x'_i} \left[h(\mathbf{x}') \int_0^t \langle K_{ij}(\mathbf{x}, t - \tau) \rangle \frac{\partial\eta^{(0)}(\mathbf{x}', \tau)}{\partial x'_j} d\tau \right]. \quad (4.18)$$

Clearly, the above equation reduces to the familiar long-wave equation in the absence of forest.

4.2. One-dimensional initial-boundary-value problem

To illustrate the complete formulation of a macro-scale problem, we consider a one-dimensional example where the sea depth is constant everywhere, i.e. $h(\mathbf{x}') = 1$. Inside the forest, $0 < x' < L'_B$, the governing equations for $\eta^{(0)}$ and $\langle u^{(0)} \rangle$ are (4.18) and (4.16), respectively. The initial condition in the forest is assumed to be

$$\eta^{(0)}(x', 0) = 0. \quad (4.19)$$

In the open water, $x' < 0$, waves can be described by

$$\eta_-^{(0)}(x', t) = \mathcal{I}(t - x') + \mathcal{R}(t + x'), \quad u_-^{(0)}(x', t) = \mathcal{I}(t - x') - \mathcal{R}(t + x'), \quad (4.20)$$

where \mathcal{I} stands for incident waves and \mathcal{R} for reflected waves. Matching the free-surface elevation and velocity at the edge, $x' = 0$, we obtain

$$\mathcal{I}(t) = \frac{1}{2} \left(\eta^{(0)}(0, t) - \int_0^t \langle K_{ij}(x, t - \tau) \rangle \frac{\partial \eta^{(0)}(x', \tau)}{\partial x'} \bigg|_{x'=0} d\tau \right), \quad (4.21)$$

and

$$\mathcal{R}(t) = \frac{1}{2} \left(\eta^{(0)}(0, t) + \int_0^t \langle K_{ij}(x, t - \tau) \rangle \frac{\partial \eta^{(0)}(x', \tau)}{\partial x'} \bigg|_{x'=0} d\tau \right). \quad (4.22)$$

Therefore, the boundary condition for $\eta^{(0)}$ at the incident edge, $x' = 0$, is

$$\eta^{(0)}(0, t) - \int_0^t \langle K_{ij}(x, t - \tau) \rangle \frac{\partial \eta^{(0)}(x', \tau)}{\partial x'} \bigg|_{x'=0} d\tau = 2\mathcal{I}(t). \quad (4.23)$$

If the forest is of finite extent L'_B , the solution in the open water on the transmission side is of the form

$$\eta_+^{(0)}(x', t) = u_+^{(0)}(x', t) = \mathcal{T}(t - x'), \quad L'_B < x' < \infty, \quad (4.24)$$

where \mathcal{T} denotes the transmitted wave. Matching the surface height and horizontal velocity at $x' = L'_B$ requires

$$\eta^{(0)}(L'_B, t) = \mathcal{T}(t - L'_B), \quad (4.25)$$

and

$$- \int_0^t \langle K(x, t - \tau) \rangle \frac{\partial \eta^{(0)}(x', \tau)}{\partial x'} \bigg|_{x'=L'_B} d\tau = \mathcal{T}(t - L'_B), \quad (4.26)$$

which can be combined to obtain the boundary condition at $x' = L'_B$,

$$\eta^{(0)}(L'_B, t) + \int_0^t \langle K(x, t - \tau) \rangle \frac{\partial \eta^{(0)}(x', \tau)}{\partial x'} \bigg|_{x'=L'_B} d\tau = 0. \quad (4.27)$$

4.3. Numerical solution for the transient conductivity

The transient cell problem for K_{ij} can be solved by the finite-element method by first rewriting the initial-boundary-value problem in the weak form. Thus, we obtain from (4.8),

$$\iint_{\Omega} \frac{\partial K_{ij}^k}{\partial x_i} \phi_j d\Omega = 0, \quad (4.28)$$

and from (4.13),

$$\iint_{\Omega} \left\{ \left[\frac{K_{ij}^k - K_{ij}^{k-1}}{\Delta t} + \frac{\partial A_j^k}{\partial x_i} + \alpha K_{ij}^k \right] \phi_{ij} + \sigma \nabla K_{ij}^k \cdot \nabla \phi_{ij} \right\} d\Omega = \sigma \oint_{s_B} \frac{\partial K_{ij}^k}{\partial n_{s_B}} \phi_{ij} ds, \quad (4.29)$$

where the index k denotes the k th time step and the time derivative is discretized by the two-point backward difference. In (4.28), summation is over the index i but not j . Again, linear triangular elements are used. The initial and boundary conditions are given in (4.11) and (4.14), respectively. In addition, (4.15) is imposed.

As an example, we consider a micro-scale geometry consisting of a circular cylinder inside a unit square as sketched in figure 1(a). Again due to micro-scale symmetry,

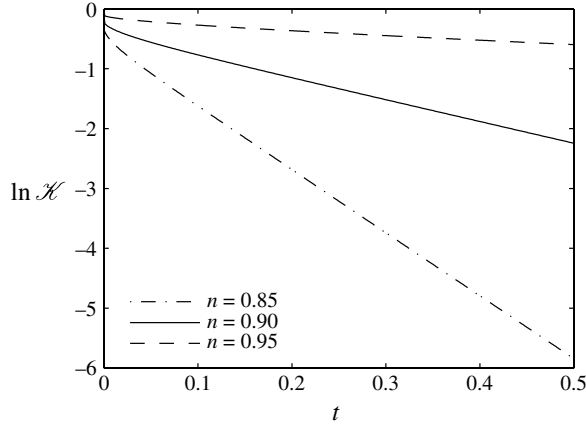


FIGURE 11. Sample solutions of $\ln \mathcal{K}(t)$ for a symmetric micro-scale configuration (see figure 1a). The corresponding controlling parameters σ and α are calculated by (2.26) and (2.29) respectively using $n = 0.85, 0.9, 0.95$ and all other parameters are listed in the third row in table 1.

$\langle K_{ij} \rangle = \mathcal{K} \delta_{ij}$ is isotropic. As shown in figure 11, our numerical results suggest that \mathcal{K} can be approximated by

$$\mathcal{K}(t) = \mathcal{K}_0 e^{-bt}, \quad (4.30)$$

where \mathcal{K}_0 and b depend on the geometry of the micro-scale problem and the controlling parameters σ and α . In particular, \mathcal{K}_0 decreases while b increases with decreasing porosity n , hence dissipation is stronger for a denser forest.

To examine the role of the cell geometry, we compare in figure 12 the conductivities of two different micro-scale configurations, i.e. one cylinder per cell vs. five per cell. Other parameters (i.e. n , α and σ , cell size) are kept the same. Note that for the same porosity, the cell with multiple cylinders has the smaller permeability. This is qualitatively consistent with the known feature in steady seepage flows (Carmen 1937), where the permeability is not only a function of porosity but also proportional to the square of the ratio $\mathcal{L} = (\text{total volume})/(\text{total surface area})$ of a grain. For circular cylindrical grains we redefine the ratio as $\mathcal{L} = (\text{total sectional area})/(\text{total circumference})$. For the single-cylinder cell, $\mathcal{L}^2 = (d/4)^2$ where d is the cylinder diameter. For the five-cylinder cell, the diameter of the four small cylinders is $d/2\sqrt{2}$, and that of the larger cylinder is $d/\sqrt{2}$. The ratio is then $\mathcal{L}^2 = (d/6\sqrt{2})^2$. This explains the large difference of conductivities.

4.4. Tsunami through a thick forest

In this section, we examine a model of the leading tsunami from a distant origin entering a forest normally. For brevity, the superscripts $^{(0)}$ and $'$ will be omitted.

While the preceding initial-boundary-value problem can be solved numerically in general, we give first an analytical solution for a semi-infinite forest with $L_B \sim \infty$ by Laplace transform. The result can be useful for physical understanding and for validating discrete computations.

Instead of (4.27), the boundary condition at $x \sim \infty$ is simply $\eta \rightarrow 0$. Taking the Laplace transform and using the convolution theorem, we obtain from (4.18) an

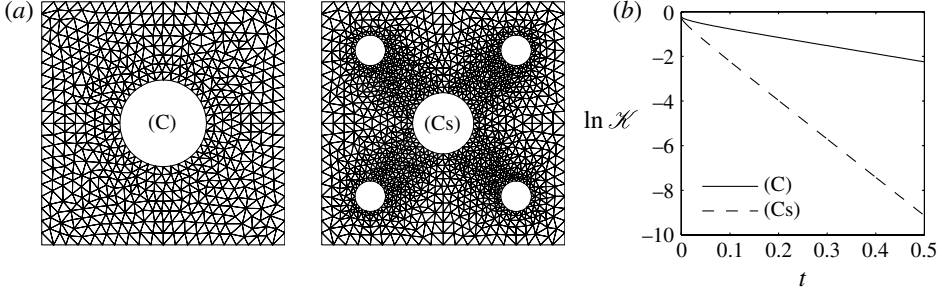


FIGURE 12. Effects of the cell geometry on the dynamic permeability, \mathcal{K} : (a) shows two different cell configurations, (b) compares the results of $\ln \mathcal{K}$. $n = 0.9$, $\sigma = 0.217$ and $\alpha = 0.0051$, which corresponds to the third row in table 1.

ordinary differential equation for the transformed free-surface displacement,

$$s\hat{\eta} = \mathcal{K} \frac{\partial^2 \hat{\eta}}{\partial x^2}, \quad x > 0, \quad (4.31)$$

where s is the transform variable and $(\hat{\cdot})$ denotes the transformed functions in s -domain. The solution satisfying the boundary condition (4.23) is

$$\hat{\eta} = \left(\frac{2}{1 + \sqrt{s\mathcal{K}}} \right) \hat{\mathcal{J}}(s) \exp \left(-x \sqrt{\frac{s}{\mathcal{K}(s)}} \right), \quad x > 0. \quad (4.32)$$

From the Laplace transforms of (4.21) and (4.22), we also obtain

$$\hat{\mathcal{R}} = \left(\frac{1 - \sqrt{s\mathcal{K}}}{1 + \sqrt{s\mathcal{K}}} \right) \hat{\mathcal{J}}. \quad (4.33)$$

It has been shown by Kajiura (1963) (see also Mei 1983, p. 31, (1.42)) that the leading tsunami from a distant and long fault line is a propagating one-dimensional wave train approximately expressed by an Airy function with amplitude decaying in time as $t^{\mu-1}$, where $\mu = 2/3$ if the seafloor rises or falls vertically (line source) and $\mu = 1/3$ if the seafloor tilts along the fault line (line dipole). For analytical convenience, we take

$$\mathcal{J}(t) = At^{\mu-1} \sin \omega t, \quad t > 0, \quad (4.34)$$

to model roughly the leading tsunami approaching the edge of the forest. The Laplace transform of (4.34) is obtained as (see Bateman 1954, p. 152, equation (15))

$$\hat{\mathcal{J}}(s) = \frac{iA}{2} \Gamma(\mu) \left[\frac{1}{(s + i\omega)^\mu} - \frac{1}{(s - i\omega)^\mu} \right], \quad (4.35)$$

in which $\Gamma(\cdot)$ denotes the Gamma function.

Assuming (4.30) for \mathcal{K} , the Laplace transform of \mathcal{K} is

$$\hat{\mathcal{K}} = \int_0^\infty dt e^{-st} \mathcal{K}_0 e^{-bt} = \frac{\mathcal{K}_0}{s + b}. \quad (4.36)$$

Consequently, the Laplace transform of the free-surface displacement in the forest is

$$\begin{aligned} \hat{\eta} = & \left(\frac{2}{1 + \sqrt{sK_0/(s+b)}} \right) \frac{i}{2} A \Gamma(\mu) \left[\frac{1}{(s+i\omega)^\mu} - \frac{1}{(s-i\omega)^\mu} \right] \\ & \times \exp \left(-x \sqrt{s(s+b)/\mathcal{K}_0} \right). \end{aligned} \quad (4.37)$$

The free-surface elevation can be obtained by inverse Laplace transform,

$$\eta = \frac{1}{2\pi i} \int_{\gamma} e^{st} \hat{\eta} ds, \quad (4.38)$$

where γ is the path parallel to the imaginary axis in the s -plane and to the right of all singularities.

It is known (Carslaw & Jaeger 1963, §126) that the asymptotic behaviour of $\eta(x, t)$ at large t can be found from its Laplace transform near the singular points with the largest real part in the complex plane of s . Leaving the details to appendix A, we only cite the results here:

$$\eta \approx \frac{2A}{t^{1-\mu}} \frac{(1 + \delta \cos \psi'') \sin(\omega t - \xi \cos \psi') - \delta \sin \psi'' \cos(\omega t - \xi \sin \psi')}{1 + 2\delta \cos \psi'' + \delta^2} e^{-\xi \cos \psi'}, \quad (4.39)$$

where

$$\xi = x \sqrt{\sqrt{\omega^2 + b^2} \frac{\omega}{\mathcal{K}_0}}, \quad \delta = \sqrt{\frac{\omega \mathcal{K}_0}{\sqrt{\omega^2 + b^2}}}, \quad \psi' = \frac{\pi + 2\psi}{4}, \quad \psi'' = \frac{\pi - 2\psi}{4}, \quad (4.40)$$

and $\psi = \tan^{-1}(\omega/b)$. Solution (4.39) represents a spatially damped progressive wave. The temporal attenuation follows the pattern of the leading wave before entering the forest.

As for the behaviour at small time, the asymptotic approximation is found from $\hat{\eta}(x, s)$ for large s (Carslaw & Jaeger 1963, §124), with the result

$$\eta(x, t) \approx \begin{cases} 0, & \text{if } x/\sqrt{\mathcal{K}_0} > t \\ \frac{2}{1 + \sqrt{\mathcal{K}_0}} A \omega \left(t - x/\sqrt{\mathcal{K}_0} \right)^\mu, & \text{if } x/\sqrt{\mathcal{K}_0} < t \end{cases} \quad (4.41)$$

as derived in appendix B. Thus the head of the tsunami enters the forest with the dimensionless speed of $\sqrt{\mathcal{K}_0}$. Since \mathcal{K}_0 is small when the porosity, n , is small, a dense forest slows the invasion of an incoming tsunami.

These approximate results are compared with the numerical solution of (4.18) by an implicit finite-difference scheme where the time derivative is approximated by the first-order backward difference and the spatial derivative by the second-order difference. A simple trapezoidal rule is used for the convolution time integral. We take the incident wave of the form (4.34) with $A = \omega = 1$ and $\mu = 2/3$ (vertical rise or fall of the seafloor). The cell geometry and controlling parameters are the same as the example of $n = 0.9$ in figure 11. For this geometry the parameter b in (4.30) is calculated to be 3.677. The asymptotic solutions for large times (4.39) and small times (4.41) are compared with discrete computation with $(\Delta x, \Delta t) = (10^{-3}, 10^{-4})$ in figures 13(a) and 13(b), respectively. Other input parameters are those listed in the third row in table 1 (i.e. $h_0 = 5$ m). In figure 13(a), which shows η at different stations for all t , the attenuation of the tsunami by the forest is clearly seen. In addition, the asymptotic approximation for large time according to (4.39) is accurate for $t > 5$.

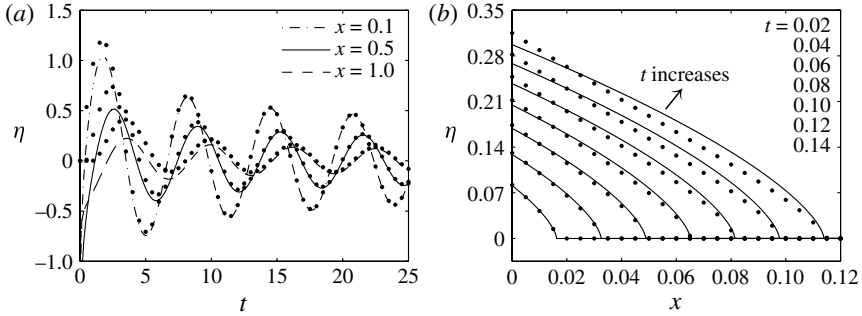


FIGURE 13. Leading waves of a tsunami entering a deep forest in a sea of constant depth: (a) time histories of free-surface elevation, η , at different stations; (b) snapshots of leading waves at initial instants of entry. Lines: asymptotic approximations. Dots: numerical solution by finite differences.

On the other hand, figure 13(b) shows that the small-time approximation according to (4.41) predicts reasonably well the leading waves entering the forest for roughly $x, t \leq 0.1$. Beyond that the discrepancy becomes more significant.

4.5. Experiments and numerical simulations for transient waves crossing a model forest

Using the same array of vertical cylinders as shown in figure 8, a series of tests has also been performed to study transient waves through the forest. Two types of long waves have been considered, namely wave packets and solitary waves. Records of free-surface elevation were recorded at the gauge stations listed in table 2. Since in shallow water ($h_0 = 0.12$ m), accurate measurement of long waves of infinitesimal steepness is difficult, most of our tests were conducted for moderately nonlinear waves. Numerical simulations were carried out by the algorithm described in § 4.4.

First we present the record of a transient wave packet consisting of a few oscillatory waves, as shown in figure 14. The packet is led by a prominent trough (depression). Data were taken at five stations as listed in table 2. Since stations G_3 and G_4 are close to the forest, data of incident and reflected waves cannot be easily separated. We use the record at G_4 (0.1 m from the leading edge of the forest) as the boundary value $\eta(0, t)$ in our numerical simulations instead of (4.23). At the exit of the forest, the boundary condition (4.27) is imposed. Bottom friction is ignored ($\alpha = 0$). The parameter $\sigma = 0.0085$ is calculated from (2.26) for $h_0 = 0.12$ m. The characteristic wave period is estimated to be 3 s and half the maximum crest-to-trough height is taken to be the wave amplitude A . Comparison between predictions and measurements at station G_5 which is at the forest centre is shown in figure 14. Spatial attenuation can be easily seen and the theory fits reasonably well with the recorded data for roughly the first 20 s. After that, reflection from the sloping beach arrived at station G_5 but is not accounted for in our simulations. Another test was performed for a packet led by an elevation. Similar agreement between data and numerical simulation is found, hence no plot is shown here.

In the next set of experiments, we generated long pulses with the profile of a soliton by displacing the piston wavemaker as a hyperbolic tangent function of time, as in Huang *et al.* (2010). Five incident waves of increasing amplitudes were tested in the same depth. The incident wave conditions are list in table 5. First we checked that the

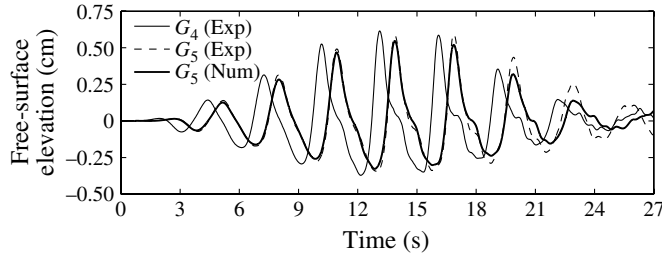


FIGURE 14. A transient wave packet crossing a forest. Solid and dashed lines: experimental data at G_4 and G_5 , respectively. Bold line: numerical prediction at G_5 .

Set	h_0 (m)	H (cm)	$1/k_0$ (m)	$k_0 L_B$	Max Re_d	σ
1	0.12	0.48	0.693	1.573	217	0.0056
2	0.12	0.93	0.498	2.190	420	0.0078
3	0.12	1.34	0.415	2.629	606	0.0094
4	0.12	1.78	0.360	3.030	850	0.0108
5	0.12	2.26	0.319	3.414	1022	0.0122

TABLE 5. Experimental conditions for solitary waves crossing a 1.08 m thick model forest with porosity $n = 0.913$. Records of corresponding free-surface elevation are shown in figures 15–17.

records at gauge G_2 agree essentially with the classical solitary wave,

$$\eta(x, t) = H \operatorname{sech}^2 \left[k_0 (x - \sqrt{g(h_0 + H)t}) \right], \quad k_0 = \sqrt{\frac{3H}{4h_0^3}}, \quad (4.42)$$

where H is the maximum wave height and k_0 the characteristic wavenumber of the soliton. Some waviness was found at the tail due to the finite increments of the step motor, and to the early stoppage of the paddle displacement. For numerical simulations the recorded time series at G_2 is used as the incident wave, $\mathcal{I}(t)$, in the boundary condition (4.23). For instance, data for $0 < t < 4.08$ s at G_2 is taken as the incident wave for Set 1 (see figure 15). During this time range reflection from the forest is not felt at G_2 , as estimated by using the wave speed of the linearized theory. In all simulations, the time origin is set at the instant when the incident wave crest reaches G_2 . Finally, (4.27) is imposed at the exit of the forest; bottom friction is ignored ($\alpha = 0$) to represent the smooth laboratory flume.

Figure 15 compares the measured and predicted free-surface elevations of two almost linear solitons with $H/h_0 = 0.04, 0.0775$ at stations G_4 , G_5 and G_6 . Reflection is computed according to (4.22). Attenuation of the advancing crest is evident at gauge G_5 at the centre of the forest, and G_6 near the exit edge. A small reflected wave is also seen at G_2 around $t = 6$ s. For larger amplitudes ($H/h_0 = 0.1117, 0.1483$), the agreement is still quite good despite the linearized approximation in the theory, as seen in figure 16. Note that the measured data show slightly higher phase speed than the prediction, and the phase difference becomes larger for higher waves. This is of course the well-known effect of nonlinearity present in the experiment but omitted in the theory.

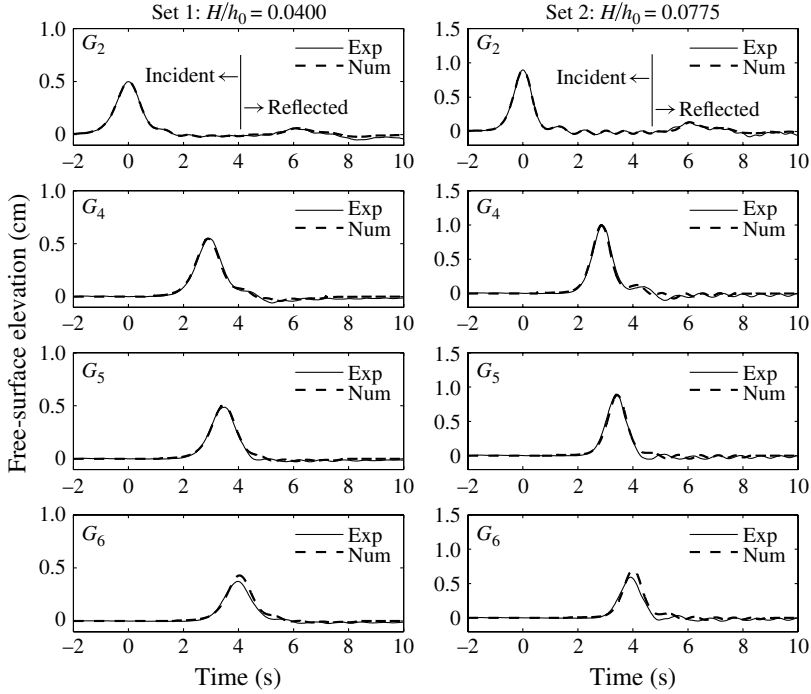


FIGURE 15. Comparison of theory (dashed lines) and measurements (solid lines) at stations: G_4 , G_5 and G_6 . Reflection from the forest is also compared at G_2 . Wave heights (H) of the incident solitary waves are 0.48 cm for Set 1 and 0.93 cm for Set 2, respectively. See figure 8 and table 2 for the positions of wave gauges.

Finally the records of a relatively large solitary wave ($H/h_0 = 0.1883$) are shown in figure 17. Strong spatial attenuation of the main crest is evident. The reflected wave with a wave height roughly 18% of the incident wave is also reasonably well predicted, as can be seen in the record at station G_2 .

5. Conclusions

Starting from a set of linearized equations we have developed a micro-mechanical theory of the attenuation of long waves by coastal forests. Modelling turbulence and bottom friction by linear terms, with the eddy viscosity taken from past experiments for steady flows, we have employed the asymptotic method of homogenization (multiple scales) to obtain the mean-field equations for the macro-scale motion. The effective conductivity for the mean-field equation is obtained by numerically solving certain canonical problems in a micro-scale cell. Analytical solutions of the macro-scale problems are discussed for sinusoidal waves. Solution of the transient problem simulating the head of a tsunami is also discussed. A series of laboratory experiments has also been conducted to study the effects of coastal forests on surface waves. In these experiments the maximum Reynolds numbers are comparable to those of the past steady-flow experiments from which the eddy viscosity is extracted. For transient long waves of finite duration, good agreement is found between numerical simulations and laboratory records of linear and even moderately nonlinear waves. For steady periodic waves the agreement is poor for very long waves due probably to beach reflection, but surprisingly good for shorter waves even when the amplitude is not very small.

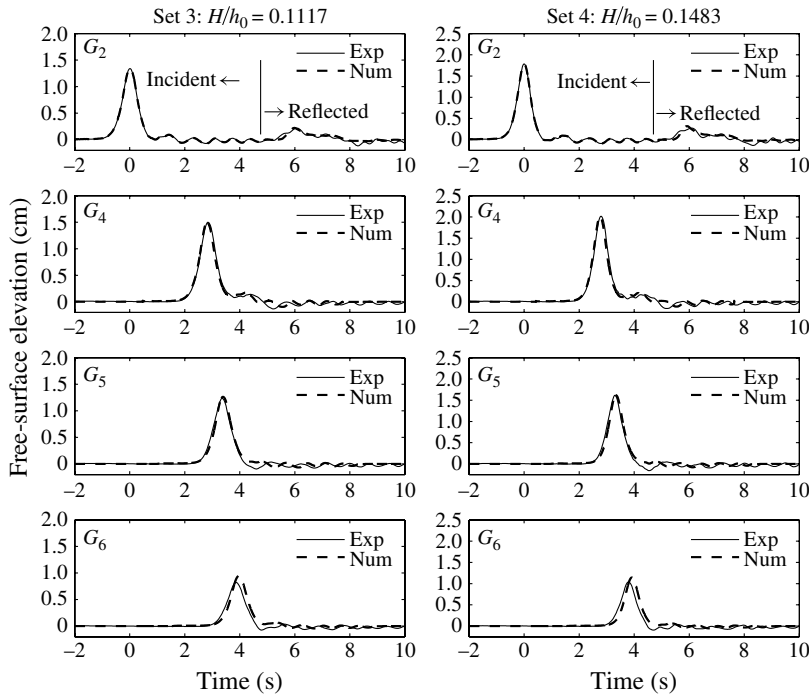


FIGURE 16. Comparison of theory (dashed lines) and measurements (solid lines) at stations G_2 , G_4 , G_5 and G_6 for both Set 3 ($H = 1.34$ cm) and Set 4 ($H = 1.78$ cm). The water depth is $h_0 = 12$ cm.

These comparisons suggest that the eddy viscosity from steady flow measurements can be used for long-wave predictions, and demonstrate the robustness of the asymptotic theory, which avoids laborious numerical computations.

In nature, the near-shore dynamics of a tsunami can of course be highly nonlinear. More experiments on wave-induced turbulence in high-Reynolds-number flows through a cylinder array are needed to provide a firmer basis for our assumptions. While it is fortunate that our linearized theory compares fairly well even for moderately short and nonlinear waves, extensions to account for nonlinearity and depth variation in shorter waves are worthwhile. The deformation of submerged plants is important for better prediction of not only the attenuation of waves but also wave-induced convective diffusion of particulates in vegetated waters. All these improvements are necessary for providing technical basis for future considerations of Green Forests for tsunami protection.

The research work presented here is supported by grants from the National Science Foundation to Cornell University. For this collaboration C.C.M. was partially funded by a Mary Upson visiting professorship from Cornell University and by the US Office of Naval Research under Grant MURI-N00014-06-1-0718.

Appendix A. Asymptotic solution for large time

The asymptotic behaviour of $\eta(x, t)$ at large t can be obtained from the inverse Laplace transform near the singularities with the largest real part in the complex

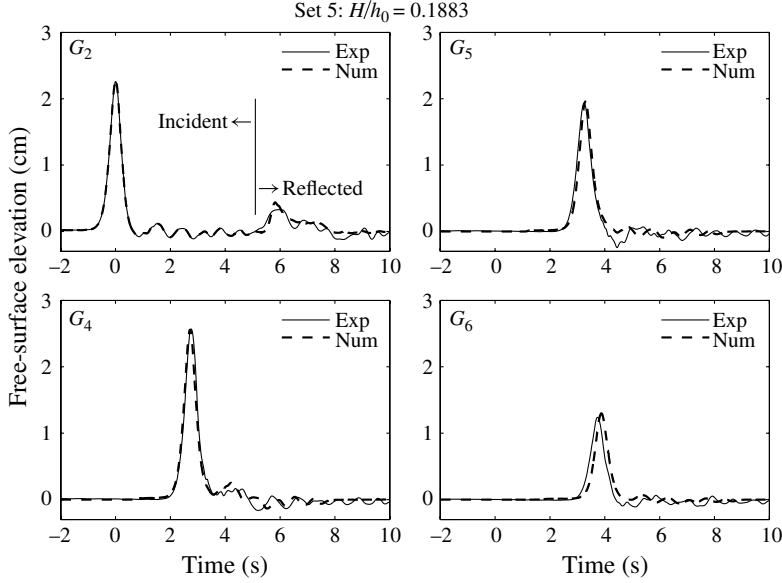


FIGURE 17. Comparison between theory (dashed lines) and measurements (solid lines) at selected stations: G_2 , G_4 , G_5 and G_6 . Wave height of the incident solitary wave is $H = 2.26$ cm and the water depth is $h_0 = 12$ cm.

plane of s (Carslaw & Jaeger 1963, p. 279). For (4.37) we shall only look at three singularities,

$$s = 0, \quad s = \pm i\omega, \quad (\text{A } 1)$$

all of which have the same real part, 0, and neglect the contribution from the pole at

$$1 + \sqrt{\frac{s\mathcal{K}_0}{s+b}} = 0, \quad \text{i.e. } s = -\frac{b}{1-\mathcal{K}_0} < 0, \quad (\text{A } 2)$$

since $\mathcal{K}_0 < 1$. The final solution is the sum of three singularities in (A 1).

Near $s = 0$, the leading term of (4.37) is

$$\begin{aligned} \hat{\eta}(x, s \approx 0) &\approx iA\Gamma(\mu) \left[\frac{1}{(i\omega)^\mu} - \frac{1}{(-i\omega)^\mu} \right] \exp\left(-x\sqrt{sb/\mathcal{K}_0}\right) \\ &= 2A\Gamma(\mu)\omega^{-\mu} \sin \frac{\mu\pi}{2} \exp\left(-x\sqrt{sb/\mathcal{K}_0}\right), \end{aligned} \quad (\text{A } 3)$$

where $\Gamma(\cdot)$ is the Gamma function. From Bateman (1954) (see p. 245, equation (1)), the inverse Laplace transform for $e^{-\sqrt{\lambda}s}$ is

$$\frac{1}{2\sqrt{\pi}} \frac{\sqrt{\lambda}}{t^{3/2}} \exp\left(-\frac{\lambda}{4t}\right). \quad (\text{A } 4)$$

Thus,

$$[\eta(x, t)]_0 \approx \frac{2}{t^{3/2}} \frac{x\sqrt{b/\mathcal{K}_0}}{2\sqrt{\pi}} \frac{A\Gamma(\mu)}{\omega^\mu} \sin \frac{\mu\pi}{2} \exp\left(-\frac{bx^2}{4\mathcal{K}_0 t}\right), \quad (\text{A } 5)$$

which dies out with t rapidly.

Next consider the singularity at $s = i\omega$. Note first

$$\exp\left(-x\sqrt{s(s+b)/\mathcal{K}_0}\right) \approx \exp\left(-x\sqrt{(i\omega)(i\omega+b)/\mathcal{K}_0}\right), \quad (\text{A } 6)$$

and

$$\sqrt{(i\omega)(i\omega+b)/\mathcal{K}_0} = e^{i(\pi/4+\psi/2)} \sqrt{\omega/\mathcal{K}_0} (\omega^2 + b^2)^{1/4}, \quad (\text{A } 7)$$

where

$$\tan \psi = \frac{\omega}{b}. \quad (\text{A } 8)$$

From Carslaw & Jaeger (1963) (see p. 280), the leading term of the inverse Laplace transform is

$$[\eta(x, t)]_{i\omega} \approx \mathcal{C}_{\mathcal{L}+} \frac{1}{t^{1-\mu}} \frac{-iA}{2} \exp\left(-xe^{i(\pi/4+\psi/2)} \sqrt{\sqrt{\omega^2 + b^2}\omega/\mathcal{K}_0}\right) e^{i\omega t}, \quad (\text{A } 9)$$

where

$$\mathcal{C}_{\mathcal{L}+} = \frac{2}{1 + \sqrt{s\mathcal{K}_0/(s+b)}} \Big|_{s=i\omega} = \left(1 + \sqrt{\omega\mathcal{K}_0/\sqrt{\omega^2 + b^2}} e^{i(\pi/4-\psi/2)}\right)^{-1}. \quad (\text{A } 10)$$

For the singularity at $s = -i\omega$, the approximate inverse Laplace transform is the complex conjugate of (A 9),

$$[\eta(x, t)]_{-i\omega} \approx \mathcal{C}_{\mathcal{L}-} \frac{1}{t^{1-\mu}} \frac{iA}{2} \exp\left(-xe^{-i(\pi/4+\psi/2)} \sqrt{\sqrt{\omega^2 + b^2}\omega/\mathcal{K}_0}\right) e^{-i\omega t}, \quad (\text{A } 11)$$

where

$$\mathcal{C}_{\mathcal{L}-} = \left(1 + \sqrt{\omega\mathcal{K}_0/\sqrt{\omega^2 + b^2}} e^{-i(\pi/4-\psi/2)}\right)^{-1}. \quad (\text{A } 12)$$

Since the contribution from $s = 0$ is relatively small at large time, we obtain $\eta \approx [\eta(x, t)]_{i\omega} + [\eta(x, t)]_{-i\omega}$ which represents a spatially damped progressive wave. The temporal attenuation follows the pattern of the leading wave before entering the forest. For good protection, the thickness of the forest should be greater than

$$O\left(\frac{1}{\sqrt{\sqrt{\omega^2 + b^2}\omega/\mathcal{K}_0}}\right), \quad (\text{A } 13)$$

which suggests that the thickness must be large for long tsunamis.

Appendix B. Asymptotic solution for small time

From Carslaw & Jaeger (1963) (see p. 274, §124), the small-time behaviour is dominated by the inverse Laplace transform at large s . For large s , (4.37) becomes

$$\begin{aligned} \hat{\eta}(s) &\approx \mathcal{C}_{\mathcal{S}} \frac{A}{2} \Gamma(\mu) \frac{i}{s^\mu} \left[\left(1 + \frac{i\omega}{s}\right)^{-\mu} - \left(1 - \frac{i\omega}{s}\right)^{-\mu} \right] e^{-sx/\sqrt{\mathcal{K}_0}} \\ &= \mathcal{C}_{\mathcal{S}} \frac{A}{2} \Gamma(\mu) \frac{i}{s^\mu} \left[\left(1 - \frac{i\mu\omega}{s}\right) - \left(1 + \frac{i\mu\omega}{s}\right) + \text{H.O.T.} \right] e^{-sx/\sqrt{\mathcal{K}_0}} \\ &= \mathcal{C}_{\mathcal{S}} \frac{A}{2} \Gamma(\mu) \left[2 \frac{\mu\omega}{s^{\mu+1}} + \text{H.O.T.} \right] e^{-sx/\sqrt{\mathcal{K}_0}}, \end{aligned} \quad (\text{B } 1)$$

where

$$\mathcal{C}_{\mathcal{S}} = \lim_{s \rightarrow \infty} \frac{2}{1 + \sqrt{s\mathcal{K}_0/(s+b)}} = \frac{2}{1 + \sqrt{\mathcal{K}_0}}. \quad (\text{B } 2)$$

Hence

$$\hat{\eta}(s) \approx \mathcal{C}_{\mathcal{S}} A \Gamma(\mu) \mu \omega \left\{ \frac{e^{-sx/\sqrt{\mathcal{K}_0}}}{s^{\mu+1}} \right\}. \quad (\text{B } 3)$$

Consider

$$\hat{\mathcal{G}}(s) = \frac{e^{-sx/\sqrt{\mathcal{K}_0}}}{s^{\mu+1}}; \quad (\text{B } 4)$$

the inverse Laplace transform is

$$\mathcal{G}(t) = \frac{1}{2\pi i} \int_{\gamma} \frac{e^{-s(x/\sqrt{\mathcal{K}_0}-t)}}{s^{\mu+1}} ds, \quad (\text{B } 5)$$

where γ is the path parallel to the imaginary axis on the s -plane and to the right of all singularities. For $x/\sqrt{\mathcal{K}_0} - t > 0$, we close the contour by a large semi circle in the right half-plane. By Cauchy's theorem and Jordan's lemma, the inverse Laplace transform is zero. Therefore, there is no disturbance if $x/\sqrt{\mathcal{K}_0} > t$.

For $x/\sqrt{\mathcal{K}_0} - t < 0$, the inverse Laplace transform is

$$\mathcal{G}(t) = \frac{1}{2\pi i} \int_{\Gamma} \frac{e^{s\xi}}{s^{\mu+1}} ds, \quad \xi = t - x/\sqrt{\mathcal{K}_0} > 0, \quad (\text{B } 6)$$

which can be evaluated as (see Bateman 1954, p. 238, (1))

$$\mathcal{G}(t) = \frac{\xi^{\mu}}{\Gamma(1+\mu)} = \frac{(t - x/\sqrt{\mathcal{K}_0})^{\mu}}{\Gamma(1+\mu)}. \quad (\text{B } 7)$$

Hence for small t ,

$$\eta(x, t) \approx \begin{cases} 0, & \text{if } x/\sqrt{\mathcal{K}_0} > t \\ \frac{2}{1 + \sqrt{\mathcal{K}_0}} A \omega (t - x/\sqrt{\mathcal{K}_0})^{\mu}, & \text{if } x/\sqrt{\mathcal{K}_0} < t, \end{cases} \quad (\text{B } 8)$$

where the property $\Gamma(1+\mu) = \mu\Gamma(\mu)$ has been evoked.

REFERENCES

- AUGUSTIN, L. N., IRISH, J. L. & LYNETT, P. 2009 Laboratory and numerical studies of wave damping by emergent and near-emergent wetland vegetation. *Coast. Engng* **56**, 332–340.
- AURIAULT, J.-L. 1980 Dynamic behavior of a porous medium saturated by a Newtonian fluid. *Internat. J. Eng. Sci.* **18**, 775–785.
- BATEMAN, H. 1954 *Table of Integral Transforms, vol. 1* (ed. A. Erdélyi). McGraw-Hill.
- CARMEN, P. C. 1937 Fluid flow through granular beds. *Trans. Inst. Chem. Engrs* **15**, 15–16.
- CARSLAW, H. S. & JAEGER, J. C. 1963 *Operational Methods in Applied Mathematics*. Dover.
- DANIELSEN, F., SØRENSEN, M. K., OLWIG, M. F., SELVAM, V., PARISH, F. & BURGESS, N. D. 2005 The asian tsunami: a protective role for coastal vegetation. *Science* **310**, 643.
- DASA, S. & VINCENT, J. R. 2009 Mangroves protected villages and reduced death toll during Indian super cyclone. *Proc. Natl Acad. Sci. USA* **106**, 7357–7360.

- ENE, H. L. & SANCHEZ-PALENCIA, E. 1975 Équations et phénomènes de surface pour l'écoulement dans un modèle de milieu poreux. *J. Méc.* **14**, 73–108.
- FERNANDO, H. J. S., SAMARAWICKRAMA, S. P., BALASUBRAMANIAN, S., HETTIARACHCHI, S. S. L. & VOROPAYEV, S. 2008 Effects of porous barriers such as coral reefs on coastal wave propagation. *J. Hydro-environ. Res.* **1**, 187–194.
- HIRAISHI, T. & HARADA, K. 2003 Greenbelt tsunami prevention in south-Pacific region. *Rep. Port and Airport Research Institute* **43** (2), 1–23.
- HUANG, Z., YAO, YAO, SIM, S. Y. & YAO, YU 2010 Interaction of solitary waves with emergent rigid vegetation. *Ocean Engng* **38**, 1080–1088.
- IRTEM, E., GEDIK, N., KABDASLI, M. S. & YASA, N. E. 2009 Coastal forest effects on tsunami run-up heights. *Ocean Engng* **36**, 313–320.
- KAJIURA, K. 1963 The leading wave of a tsunami. *Bull. Earthq. Res.* **41**, 525–571.
- KELLER, J. B. 1980 Darcy's law for flow in porous media and the two-space method. In *Nonlinear Partial Differential Equations in Engineering and Applied Science* (ed. R. L. Sternberg *et al.*). *Lecture Notes in Pure and Applied Mathematics*, vol. 54. pp. 429–443. Dekker.
- KELLER, J. B. & KELLER, H. B. 1964 Water wave run-up on a beach. *ONR. Res. Rep.* Contract No. NONNR-3828(00), Department of the Navy.
- KOBAYASHI, N., RAICHLEN, A. W. & ASANO, T. 1993 Wave attenuation by vegetation. *J. Waterways Port Coast. Ocean Engng* **119**, 30–48.
- LIU, P. L.-F., LYNETT, P., FERNANDO, H., JAFFE, B. E., FRITZ, H., HIGMAN, B., MORTON, R., GOFF, J. & SYNOLAKIS, C. 2005 Observations by the international tsunami survey team in Sri Lanka. *Science* **308**, 1595.
- MAZDA, Y., KOBASHI, D. & OKADA, S. 2005 Tidal-scale hydrodynamics within mangrove swamps. *Wetlands Ecol. Manage.* **13**, 647–655.
- MASSEL, S. R., FURUKAWA, K. & BINKMAN, R. M. 1999 Surface wave propagation in mangrove forests. *Fluid Dyn. Res.* **24**, 219–249.
- MEI, C. C. 1983 *The Applied Dynamics of Ocean Surface Waves*. Wiley.
- MEI, C. C. & VERNESCU, B. 2010 *Homogenization Methods for Multiscale Mechanics*. World Scientific.
- MÖLLER, I. 2006 Quantifying saltmarsh vegetation and its effect on wave height dissipation: results from a UK East coast saltmarsh. *Estuar. Coast. Shelf Sci.* **69**, 337–351.
- MÖLLER, I., SPENCER, T., FRENCH, J. R., LEGGETT, D. J. & DIXON, M. 1999 Wave transformation over salt marshes: a field and numerical modelling study from North Norfolk, England. *Estuar. Coast. Shelf Sci.* **49**, 411–426.
- NEPF, H. M. 1999 Drag, turbulence, and diffusion in flow through emergent vegetation. *Water Resour. Res.* **35**, 479–489.
- NIELSEN, P. 1992 *Coastal Bottom Boundary Layers and Sediment Transport*. World Scientific.
- PHILLIPS, O. M. 1977 *Dynamics of the Upper Ocean*. Cambridge University Press.
- SHENG, P. & ZHOU, M. Y. 1988 Dynamic permeability of porous media. *Phys. Rev. Lett.* **61**, 1951–1954.
- SUZUKI, T., DIJKSTRA, J. & STIVE, M. J. F. 2008 Wave dissipation on a vegetated salt marsh. *Proc. Intl Conf. Coast. Engng* 331–339.
- SWART, D. H. 1974 Offshore sediment transport and equilibrium beach profiles. *Delft Hydr. Lab. Publ. No.* 131.
- TANAKA, N., SASAKI, Y., MOWJOOD, M. I. M., JINADASA, K. B. S. N. & HOMCHUEN, S. 2007 Coastal vegetation structures and their function in tsunami protection: experience of the recent Indian Ocean tsunami. *Landscape Ecol. Engng* **3**, 33–45.
- THUY, N., TANIMOTO, K., TANAKA, N., HARADA, K. & IIMURA, K. 2009 Effect of open gap in coastal forest on tsunami run-up – investigations by experiment and numerical simulation. *Ocean Engng* **36**, 1258–1269.
- WOLANSKI, E. 1992 Hydrodynamics of mangrove swamps and their coastal waters. *Hydrobiologia* **247**, 141–161.
- WOLANSKI, E., JONES, M. & BUNT, J. S. 1980 Hydrodynamics of a tidal creek-mangrove swamp system. *Austral. J. Mar. Freshwat. Res.* **31**, 431–450.
- ZHOU, M. Y. & SHENG, P. 1989 First-principle calculation of dynamic permeability of porous media. *Phys. Rev. B* **39**, 12027–12039.